Sea waves impact on turbulent heat fluxes in the Barents Sea according to numerical modeling

Stanislav Myslenkov[1,2,3] Anna Shestakova[4], Dmitry Chechin[4,5]

[1]Lomonosov Moscow State University, 119991, Moscow, Russia

[2]Shirshov Institute of Oceanology RAS, 117997, Moscow, Russia

[3]Hydrometeorological Research Centre of the Russian Federation, 123242, Moscow, Russia

[4]A.M.Obukhov Institute of Atmospheric Physics RAS, 119017, Moscow, Russia

[5]Moscow Institute of Physics and Technology, 119017, Moscow, Russia

Correspondence to: Stanislav Myslenkov (stasocean@gmail.com)

Abstract. This paper investigates the impact of sea waves on turbulent heat fluxes in the Barents Sea. The COARE algorithm, meteorological data from reanalysis and wave data from the ~~WW3~~ WWIII wave model results were used. The turbulent heat fluxes were calculated using the modified Charnock parameterization for the roughness length and several parameterizations, which explicitly account for the sea waves parameters. A catalog of storm wave events and a catalog of extreme cold-air outbreaks over the Barents Sea were created and used to calculate heat fluxes during extreme events.

The important role of cold-air outbreaks in the energy exchange between ~~of~~ the Barents Sea and the atmosphere is demonstrated. A high correlation was found between the number of cold-air outbreaks days and turbulent fluxes of sensible and latent heat, as well as with the net flux of long-wave radiation averaged over the ice-free surface of the Barents Sea during a cold season.

The differences in the long-term mean values of heat fluxes calculated using different parameterizations for the roughness length are small and are on average 1-3% of the flux magnitude. Parameterizations of Taylor and Yelland and Oost et al. on average lead to an increase of the magnitude of the fluxes, and the parameterization of Drennan et al. leads to a decrease of the magnitude of the fluxes over the entire sea compared to the Charnock parameterization.

The magnitude of heat fluxes and their differences during the storm wave events exceed the mean values by a factor of 2. However, the effect of explicit accounting for the wave parameters is, on average, small and multidirectional, depending on the used parameterization for the roughness length. In the climatic aspect, it can be argued that the explicit accounting for sea waves in the calculations of heat fluxes can be neglected.

However, during the simultaneously observed storm waves and cold-air outbreaks, the sensitivity of the calculated values of fluxes to the used parameterizations increase along with the turbulent heat transfer increase. In some extreme cases, during storms and cold-air outbreaks, the difference ~~exceeds~~reaches 700 W m^{-2}.

Keywords: Barents Sea; turbulent heat flux; Charnock parameter; COARE; wind wave hindcast; cold-air outbreaks

1. Introduction

Atlantic water undergoes a significant transformation in the Barents Sea where its characteristics, such as temperature, salinity and density, change. New water masses are formed which contain different volumes of the original Atlantic water (Ivanov and Timokhov, 2019). A significant part of the heat content of Atlantic water is spent on melting ice and heating the atmosphere influencing the climatic characteristics of the region (Rahmstorf and Ganopolski, 1999). To a large extent, the heat exchange between the Barents Sea and the atmosphere is carried out by the turbulent heat flux. The Barents Sea is known to be one of the most efficient heat sinks from the ocean to the atmosphere (Simonsen and Haugan, 1996). On average, turbulent heat transfer in the Barents Sea is about 30 W/m2, according to modeling data (Arthun and Schrum 2010). However, even rough reanalysis data show that in energy active zones near the ice edge, fluxes can reach 500 W/m2 (Hakkinen and Cavalieri 1989). The latter depends on the surface roughness, which is associated with the wind wave parameters. Thus, adequate representation of surface roughness is crucial for correct estimates of the surface heat flux.

The modern models of the atmosphere and ocean commonly use the Charnock formula (Charnock, 1955) as a parameterization of the aerodynamic roughness length over the water. The Charnock relationship represents a quadratic dependence of the roughness length on the friction velocity. The Charnock parameter as constant, which represents the proportionality coefficient between the roughness length and the square of friction velocity, used in the most frequently models and reanalyses (for example, in NCEP/NCAR, NCEP/CFSR, MERRA reanalyses). However, numerous studies of roughness behavior in different conditions according to observational data (e.g. Oost et al. 2002, Mahrt et al. 2003) showed that the Charnock parameter (coefficient) is not constant, especially in conditions of high wind speed and high waves. The Charnock formula is applicable when the wave state is in equilibrium with wind forcing, and does not take into account the age of the waves and such effects as wave breaking and spray formation.

Thereby, several parametrizations were proposed that explicitly or implicitly take into account the influence of such wave parameters as wave height, wave length and period on the sea surface roughness.

In the most simple modification of the Charnock formulation the Charnock parameter is set as a piecewise constant or a linear function of wind speed in order to fit the observations. In other parametrizations, the Charnock parameter explicitly depends on the wind wave parameters, usually the wave steepness (Taylor and Yelland 2001) and wave the age (Jones and Toba 2001, Oost et al. 2002, Drennan et al. 2003). More complex parameterizations are based on the relation between the roughness length and the wave momentum flux (Janssen 1991) and are typically used in coupled wave-atmosphere models, including ECMWF operational analysis and reanalyses (ECMWF 2007). Intercomparisons of different roughness parametrizations, including Taylor and Yelland (2001), Oost et al. (2002) and Drennan et al. (2003) parametrizations, did not reveal the best of them (Pan et al. 2008, Charles and Hemer 2013, Shimura et al. 2017, Kim et al. 2018, Prakash et al. 2019). Some studies have shown that Oost et al. parametrization overestimates the roughness of the sea surface in comparison with other schemes (Pan et al. 2008, Kim et al. 2018), and Drennan et al. parametrization usually gives a lower roughness (Charles and Hemer 2013).

The choice of roughness length parameterization affects primarily the momentum flux and turbulent heat transfer. The sensible and latent heat fluxes are calculated using ~~also~~ the roughness length for temperature and specific humidity, respectively. The ratio of the roughness lengths for scalars and momentum is typically parameterized as function of the Reynolds roughness number (Brutsaert 1982, Zilitinkevich et al. 2001, Renfrew et al. 2002, Brunke et al . 2011).

The turbulent heat transfer in most reanalyses is parameterized using bulk formulae. ~~in most reanalyses, which differ in~~ ~~t~~The choice of the parameterization for the roughness length for temperature and humidity, parameterization of the Charnock parameter, and of the universal functions describing the dependence of the transfer

80 coefficients on the surface layer stratification (Renfrew et al. 2002, Brunke et al. 2011). A list of the parameterizations
81 used in the ~~main~~ different reanalyses is given in the Appendix by Brunke et al. (2011).

82   The use of certain parameterization can significantly affect the value of the calculated heat and momentum
83 fluxes. For instance, the difference in the total turbulent heat flux between the two most commonly used algorithms,
84 NCAR (Large and Yeager, 2009) and COARE (Coupled Ocean Atmosphere Response Experiment) (Fairall et al.
85 1996), is 13 W/m^2 on average throughout the globe and reaches 15-20% of the flux magnitude in mid-latitudes and
86 subpolar regions (Brodeau et al. 2017). Typical values of the average difference of turbulent fluxes produced by
87 different algorithms and the observational data amount to 5-15 W/m^2. Unambiguously "the best set of
88 parameterizations" of the roughness length and universal functions for calculating heat and momentum fluxes does
89 not exist (Brunke et al. 2011;, Charles and Hemer 2013). Nevertheless, the widely used COARE algorithm (Fairall et
90 al. 1996, Fairall et al. 2003), which is also embedded in satellite flux calculation algorithms, is considered the most
91 reliable for calculating turbulent fluxes. Satellite products such as J-OFURO, HOAPS, and OAFlux (joint satellite and
92 simulation product), use algorithms very similar to COARE (Brunke et al. 2011, Yu et al. 2011). The COARE
93 algorithm offers a choice of Taylor and Yelland (2001) and Oost et al. (2002) roughness length parameterizations,
94 which explicitly take into account the wind wave parameters.

95   Roughness length dependency on wind wave parameters is expected to have regional differences depending
96 on the local features of the wave regime. According to studies ~~of the wave climate of the Barents Sea~~ (Wind and
97 Wave…, 2003; Stopa et al., 2016; Liu Q. et al., 2016), a ~~significant part of the year stormy~~ strong winds and high
98 waves observed in the Barents Sea most of the year. ~~weather prevails over the Barents Sea.~~ The duration of periods in
99 which the wind speed does not exceed 15 m/s in the winter months averages only 3–6 days. The mean wave height
100 (probability of exceedance 50%) with a frequency of occurrence of 1 time per year is 6.1 m, and the maximum wave
101 height (probability of exceedance 0.1%) is more than 19 m (Wind and Wave…, 2003). Such values indicate the high
102 frequency of occurrence of extreme waves. The average significant wave heights of in the Barents Sea is 1.8–2.2 m
103 for the central part of the Barents Sea (Myslenkov et al., 2019). The maximum of significant wave heights reaches
104 12–14 m in the central part of the Barents Sea. The storms with significant wave heights of more than 4 m are
105 observed on average 70–80 times a year, with significant wave heights more than 5 m - 40–60 times a year. The
106 interannual variability of the recurrence of storm waves is very large (for different years the number of cases can vary
107 by a factor of 2–3) (Myslenkov et al., 2018, 2019).

108   Moreover, the wave climate of the Barents Sea is characterized by a significant influence of swell coming
109 from the North Atlantic. Based on numerical experiments (Myslenkov et al., 2015), it was shown that the height of
110 swell can reach 5 m with a period of 15-18 sec. The effect of swell is not taken into account in the Charnock
111 relationship explicitly, which can cause errors in the calculated values of the roughness length and turbulent fluxes.

112   In addition to wind speed, the difference of temperature and specific humidity between the sea surface and air
113 also affects the magnitude of turbulent heat fluxes over the sea. These differences reach particularly large values
114 during the so-called cold-air outbreaks (CAOs). CAOs represent the advection of a dry and cold air mass onto the
115 open sea originating from the Central Arctic or from the cold continents (Pithan et al., 2018). The temperature
116 difference between water and air during CAOs can exceed 30 °C near the marginal sea ice zone, and the maximum
117 values of the total turbulent heat flux can exceed 600 W/m^2 (Brümmer, 1996). As the air mass warms and moistens
118 with increasing distance from the ice edge, the total heat flux decreases. The horizontal scale of the air mass
119 transformation is about 500-1000 km for typical CAOs (Chechin and Lüpkes, 2017). Thus, large areas of the non-
120 freezing seas, such as the Barents Sea, are subject to intense heat loss. The heat loss due to CAOs can reach up to 60%
121 over the Greenland and Iceland Seas (Papritz and Spengler, 2017), although the specific value depends on the criteria
122 used for the identification of CAOs. To our knowledge, no systematic study of the the CAOs role in the air-sea heat

123 exchange exists for the Barents Sea, although the importance of CAOs has been stressed earlier (Smedsrud et al.,
124 2013).

125   Furthermore, CAOs create favorable conditions for enhancing wind speed over water, which leads to further
126 intensification of the energy exchange. The wind speed increase is primarily associated with the formation of large
127 horizontal temperature gradients and strong baroclinicity. This can lead to the intensification of cyclones and
128 mesocyclones (Kolstad, 2015), formation of jets and wind shear along the lower tropospheric fronts (Grønas and
129 Skeie, 1999), convergence lines (Savijärvi, 2012), and low-level jets (Brümmer 1996; Chechin et al., 2013; Chechin
130 and Lüpkes, 2019). Although the highest wind speeds over the Barents Sea have the orographic origin (e.g., the
131 Novaya Zemlya Bora (Moore, 2013)), it was shown (Kolstad, 2015) that in cyclones, the wind speed reaches its
132 maximum value when intense cold advection takes place in their rear part. In addition, intense turbulent exchange in
133 the convective boundary layer effectively transports momentum down to the lower atmospheric layer increasing the
134 near-surface wind speed (Chechin et al., 2015).

135   In this paper, we consider the influence of sea waves on turbulent heat fluxes in the Barents Sea. Heat fluxes
136 were calculated using the COARE 3.0 algorithm and NCEP/CFSR reanalysis data with the Charnock roughness
137 length parameterization and parameterizations explicitly taking into account the parameters of sea waves - Taylor and
138 Yelland (2001), Oost et al. (2002) and Drennan et al. (2003). The results were verified by the ship measurements of
139 turbulent heat fluxes obtained during the NABOS (Nansen and Amundsen Basins Observational System) campaigns
140 in different years. The wind wave parameters were obtained from the WaveWatchIII (WWIII) wave model. Special
141 attention is paid to the cases of intense storms and cold-air outbreaks events, when the expected difference between
142 calculations with different roughness parameterizations is the largest.

143

144 **2. Data and Methods**

145

146 **2.1 Wave modeling**

147   The wave characteristics in the Barents Sea were computed using the spectral wave model WaveWatchIII
148 (WWIII) version 4.18. The ~~WW3~~ WWIII model is a~~n~~ development of the WAM model with regard to the functions of
149 the source and the nonlinear interaction (Tolman, 2014). This model is based on a numerical solution of the equation
150 of the spectral wave energy balance

151 $$\frac{\partial E(\omega, \theta, \vec{x}, t)}{\partial t} + \vec{V}(\omega, \theta)\nabla E = S(\omega, \theta, \vec{x}, t),\qquad(1)$$

152   where ω and θ are the frequency and the propagation direction of the spectral component of the wave energy;
153 $E(\omega, \theta, \vec{x}, t)$ is the two-dimensional spectrum of the wave energy at a point with vector coordinate $\vec{x}$ at time
154 point t; $\vec{V}(\omega, \theta)$ is the group velocity of the spectral components; $S(\omega, \theta, \vec{x}, t)$ is a function that describes
155 the wave energy sources and sinks, i.e., the transfer of the energy from the wind to the waves, nonlinear wave
156 interactions, dissipation of the energy through collapse of the crests at a great depth and in the coastal zone, friction
157 against the bottom and ice, wave scattering by ground relief forms, and reflection from the coastline and floating
158 objects. The energy balance equation is integrated using finite-difference schemes by the geographic grid and the
159 spectrum of wave parameters.

160   In this work, the computations were made using the ST1 scheme (Tolman, 2014). To account for the
161 nonlinear interactions of the waves, the Discrete Interaction Approximation (DIA) model (Hasselmann and

162 Hasselmann, 1985) was used, which is a standard approximation for calculation of nonlinear interactions in all
163 modern wave models.

164   To take into account ice effects on the wave development, the IC0 scheme was used, where the grid point is
165 considered as ice-covered if the ice concentration was larger than 0.25. Thus, the exponential attenuation of wave
166 energy adjusted for the sea ice concentration at a given point was added.

167   In the shallow water, the increase in wave height as waves approach the shore and the related wave breaking
168 after waves reach the critical value of steepness were taken into consideration. The whitecapping effect taken into
169 account in the ST1 scheme. The standard JONSWAP scheme was used to take the bottom friction into account. The
170 spectral resolution of the model is 36 directions (Dq = 10°), the frequency range consists of 36 intervals (from 0.03 to
171 0.843 Hz).

172   The calculations were performed using the original unstructured grid, which is based on the bottom
173 topography data from ETOPO1 database and detailed nautical charts (Figure 1). This unstructured grid consists of
174 16792 nodes; the spatial resolution varies from 15 km for the open part of the Barents Sea to 500 m for the coastal
175 regions. The computational domain of the model covers the Barents and the Kara Seas and the entire northern part of
176 the Atlantic Ocean (Figure 1). Previously, this grid was successfully used for wave modeling (Myslenkov et al., 2018;
177 Myslenkov et al., 2019). The need to take into account the swell propagating from Atlantic ocean when calculating the
178 height of significant waves in the Barents Sea was clearly shown in the previous work of the authors (Myslenkov et
179 al., 2015).
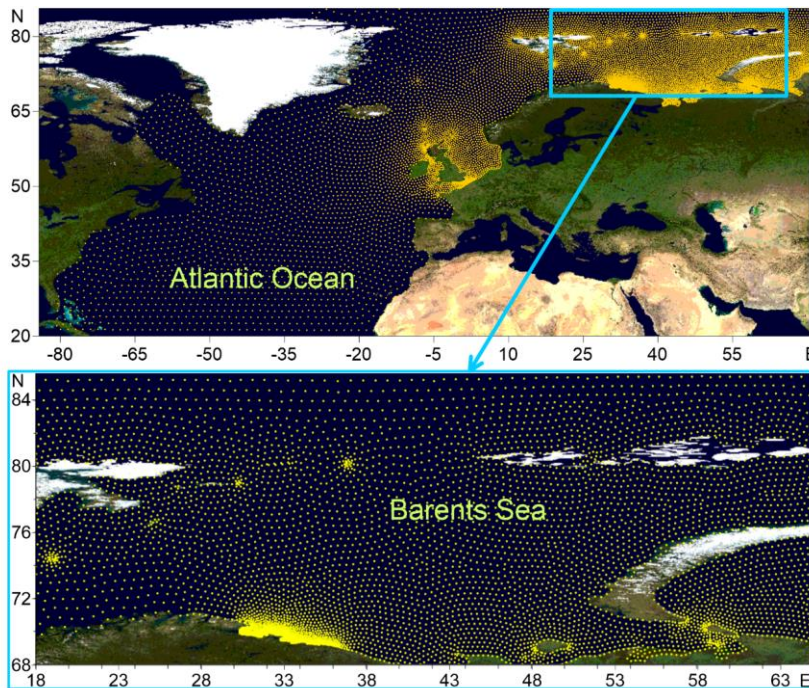
180
181   Figure 1. The computational unstructured grid for the Atlantic Ocean and the Barents Sea. The base map is
182 the Blue Marble which obtained by connecting to the WMS demo server in the Surfer Golden Software program.
183

184   The general time step for the integration of the full wave equation was 15 minutes, the time step for the
185 integration of functions of sources and sinks of wave energy was 60 s, the time step for the spectral energy transfer
186 and for satisfying the Courant–Friedrichs–Lewy condition was 450 s. This choice is dictated by the configuration of
187 the computational grid: the maximum and minimum distances between the nodes and a large latitudinal extent.

188   The 10-m wind from the NCEP/CFSR reanalysis (Saha et al., 2010) for the period of 1979 to 2010 with the
189 spatial resolution of ~0.3° was used as the forcing. Data of NCEP/CFSv2 reanalysis (Saha et al., 2014) with the
190 resolution of ~0.2° and with the time step of 1 hour were used for the period of 2011 to 2017.

191   The wave model quality assessments based on Cryosat satellite data for period 2010-2017 (data collected
192 from IMOS satellite database (Ribal and Young, 2019)). A comparison of the modeled and satellite SWH is shown on
193 Figure 2. The model calculations provides the R (correlation coefficient) is 0.88, the BIAS is -0.04 m, and the RMSE
194 is 0.53 m. The Scatter Index is 0.28. The results of quality assessments based on the satellite data is similar to other
195 assessments (Li et al., 2019, Stopa et al., 2016).
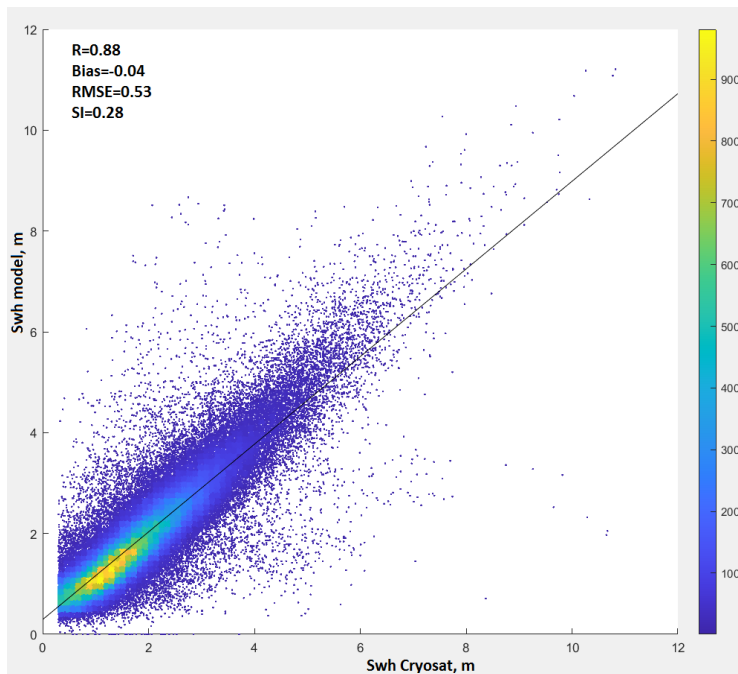
197 Figure 2. Scatter diagram of model SWH and satellite data.

200   In this paper, we used the output results of the wave model with time step 3 hours from 1979 to 2017 for each
201 node of the unstructured grid.

202   Based on the wave model results, a study of storm activity was carried out according to the POT (Peak Over
203 Threshold) method which used successfully earlier in (Myslenkov et al., 2019). For each year in the Barents Sea, the
204 number of storm surges with different significant wave heights from 5 to 8 m was calculated. The event is counted as
205 the storm with wave height > 5 m if at least in one node in the study area the wave height exceeds the threshold of 5 m
206 This event continues until the wave height at all nodes becomes less than the threshold. To eliminate possible errors,

207 at least 9 hours should pass between two storm events. Using the described procedure, a catalog of storm days was
208 compiled when the significant wave heights of more than 5 m were observed. A total of 1964 days were identified for
209 the period 1979-2017.

210

211 **2.2 COARE algorithm and parameterizing the roughness parameter**
212 Turbulent heat fluxes were calculated using the COARE algorithm (Fairall et al., 1996), based on the LKB
213 model (Liu et al., 1979). Bulk formulae for the momentum and scalar fluxes have the general form:

214 $$w'x' = c_x^{1/2} c_d^{1/2} S\Delta X = C_x S\Delta X,$$ (2)

215 where w' is the fluctuations of vertical wind, x can be a is the horizontal wind components u, v, temperature
216 or specific humidity, c_x – transfer coefficients for x, c_d – transfer coefficient for momentum, C_x – total transfer
217 coefficient, ΔX – the difference the mean x at a height equal to the roughness length and at a certain height (10 m) in
218 the atmospheric surface layer (Fairall et al., 2003). S – mean wind speed with gusts U_g:

219 $$S = \sqrt{U^2 + V^2 + U_g^2}$$

220 The default value of U_g is 0.5 m/s in the COARE algorithm. Transfer coefficients depend on the roughness
221 length and dimensionless universal functions. The form of universal functions in the COARE algorithm is set in
222 accordance with (Beljaars and Holtslag, 1991) for stable stratification; the so-called Kansas functions (Kaimal et al.,
223 1972) are used for unstable stratification; functions from Fairall et al. (1996) and Grachev et al. (2000) are used for
224 very unstable stratification. For the roughness length, several parameterizations are available in the COARE
225 algorithm. The parameterization of Charnock (Charnock, 1955) implies dependence of roughness on the friction
226 velocity u_*:

227 $$z_0 = \frac{\alpha u_*^2}{g} + \frac{0.11a}{u_*}$$ (3)

228 where α – Charnock parameter, g – gravity acceleration, a – kinematic viscosity coefficient (Andreas, 1989).
229 Equation (3) is the modified Charnock formula (Smith, 1988), in which the second term on the right side describes the
230 roughness over an aerodynamically smooth surface (i.e., in weak winds). The Charnock coefficient is set piecewise
231 constant in strong and weak winds and linearly dependent on 10-m wind speed in moderate winds:

$$\begin{cases} 0.011, & S < 10 \ m/s \\ 0.011 + \dfrac{0.007(S-10)}{8}, & 10 \ m/s < S < 18 \ m/s \\ 0.018, & S > 18 \ m/s \end{cases}$$

232
233

234 In the parameterization of Taylor and Yelland (2001) (hereafter - T1), the roughness length is related to the
235 wave steepness (H_s/L_p):

236 $$z_0 = H_s a_1 \left(\frac{H_s}{L_p}\right)^{b_1} + \frac{0.11a}{u_*}, \quad a_1 = 1200, \quad b_1 = 4.5$$ (4)

237 where H_s – significant wave height, L_p – spectral peak wavelength.

238 The parameterization of Oost et al. (2002) (hereafter - O2) implies the dependence of the roughness length on
239 the spectral peak wavelength L_p and inverse wave age (Uu_*/c_p):

240 $$z_0 = L_p a_2 \left(\frac{u_*}{c_p}\right)^{b_2} + \frac{0.11a}{u_*}, \quad a_2 = 50/2\pi, \quad b_2 = 4.5$$ (5)

241   Here c_p –phase wave speed associated with spectral peak, which is expressed through the wave length as

242    $c_p = \sqrt{L_p g / 2\pi}$.

243   Finally, we included the parametrization of Drennan et al. (2003) (hereafter - D3) in the COARE algorithm.
244   D3 parameterization consists in the dependence of the roughness length on the wave height and inverse wave age:

245    $$z_0 = H_s a_3 \left(\frac{u_*}{c_p}\right)^{b_3} + \frac{0.11a}{u_*}, \quad a_3 = 3.35, \quad b_3 = 3.4 \tag{6}$$

246   Thus, the main components of the algorithm are the equation (2), formulae for calculating transfer
247   coefficients based on the Monin-Obukhov similarity theory, and formulae (3-6) for the roughness length. Thus, in
248   general, the COARE algorithm is similar to corresponding algorithms in most atmospheric models.
249   Using the COARE algorithm, we calculated turbulent sensible and latent heat fluxes in the Barents Sea from
250   1979 to 2017. Mean fluxes were calculated for long-term period and for periods of cold-air outbreaks and storm wave
251   events. Since the scatter index of our modeled significant wave heights is 0.28 (or 28%), then probably this value can
252   lead to mean errors ~4-5% in the calculated heat flux values.

253
254   **2.3 Input data for the COARE algorithm**

255   Input data for the COARE algorithm are: wind vector, air temperature, sea surface temperature (SST), air
256   humidity, incoming short-wave and long-wave radiation, precipitation intensity, sea wave height and period.
257   NCEP/CFSR and CFSv2 (Saha et al., 2010, 2014) reanalysis with temporal resolution of 6 hours and total period
258   1979-2017 were used as atmospheric data input for the COARE algorithm–. CFSv2 reanalysis data for the period
259   2011-2017 (with a slightly better spatial resolution than CFSR, were interpolated from the ~0.2˚ grid to ~0.3˚ grid to
260   match the CFSR resolution. The wind speed was used at 10 m height, air temperature and humidity were used at 2 m
261   height. Reanalysis data are also available at isobaric levels, the lower of which is 1000 hPa. However, we preferred to
262   take diagnostic variables at heights of 2 and 10 m for several reasons. Firstly, the height of the isobaric levels varies
263   greatly and the lower available level may be at a high height (above the boundary layer). Secondly, data at vertical
264   levels are available on a much coarser grid (0.5 °). For instance, Arthun and Schrum (2010) also used diagnostic
265   variables at standard levels from the NCEP-NCAR reanalysis to calculate turbulent fluxes in the ocean model. The
266   surface pressure and the inversion height (boundary layer height), which are usually set constant in the COARE
267   algorithm, were set from the CFSR reanalysis (at each moment of time and at each grid point).

268
269   **2.4 Ship observations**
270   We used ship observations in the Barents Sea from the NABOS expeditions in 2005, 2007, 2013, and 2015 to
271   verify turbulent heat fluxes calculated using the COARE algorithm. All expeditions took place in a period from
272   August to October. Ship-borne fluxes were calculated using the eddy-covariance method (the left side of equation (2))
273   based on high-frequency measurements of temperature and the three wind components using Gill and Metek sonic
274   anemometers (Ivanov et al., 2019; Varentsov et al., 2016). The averaging period for the covariance calculations was
275   10 min. For all wind measurements, a correction was made for the movement of the ship. A detailed description of the
276   location of the instruments and methods of filtering data and calculating fluxes is available at https://uaf-
277   iarc.org/nabos-cruises/. For verification, the calculated values of heat fluxes were bilinearly interpolated (using 4
278   surrounding points)- from the CFSR reanalysis grid to the observation points.

279
280   **2.5. Identification of CAOs**

281   The so-called «CAO index» is frequently used for CAO identification. It was first defined (Kolstad and

282 Bracegirdle, 2008; Kolstad et al., 2009) as the potential temperature difference between the ocean surface and the 700

283 hPa height normalized by the pressure difference at the same heights. The authors used the value of the 90th

284 percentile of the CAO index to estimate the strength and frequency of occurrence of CAOs. Other investigators (e.g.,

285 Fletcher et al., 2016) used the non-normalized potential temperature difference between the surface and the 800hPa

286 height. As metrics to study the frequency and strength of CAOs they evaluated the frequency of occurrence of the

287 positive values of the CAO index, as well as the value of the 95th percentile of the CAO index during the winter

288 months.

289   Here, we define the CAO index I_{cao} as the daily potential temperature difference between the ocean surface

290 and the 700 hPa height. For each day, I_{cao} was averaged over the ice-free part of the Barents sea. Figure 2 3 shows the

291 obtained I_{cao} values for the period 1979-2018. Solid curve on Figure 2 3 consists of the multiyear-averaged values

292 $\overline{I_{CAO}}$ obtained by 1) averaging I_{cao} over a 30-day period centered on the given day and 2) averaging the obtained

293 values over the years. Similarly, the standard deviation σ_I of I_{cao} was obtained.

294
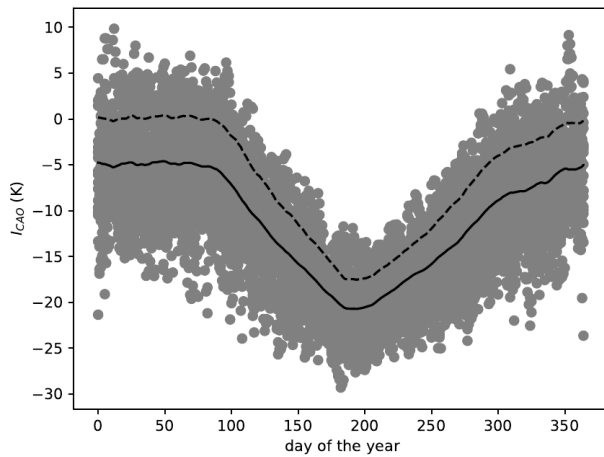
295   Figure 2 3. Cold-air outbreak index I_{cao} for the period 1997-2017. Solid curve represents the 30-day running

296 multiyear mean values $\overline{I_{CAO}}$. Extreme CAOs correspond to points above the dashed curve which is the sum $\overline{I_{CAO}}$

297 $+ \sigma_I$ where the latter is the 30-day running multiyear standard deviation of I_{cao}.

298

299   The dashed curve in Figure 2 3 represents the threshold value $\overline{I_{CAO}} + \sigma_I$ which we use as a criteria for

300 CAO identification, namely

301 $$I_{CAO} > \overline{I_{CAO}} + \sigma_I \qquad\qquad (7)$$

302   According to the criteria (7), we identify CAOs as those cases when I_{cao} values are above the dashed curve in

303 Figure 2 3. A similar procedure was used in other studies (e.g., Wheeler et al., 2011) to identify continental CAOs

304 where authors used simply the air temperature at 2 m height instead of I_{cao}.

305   Figure 2 3 shows that the largest values of I_{cao} are observed in a period from the second half of December
306   until the end of March when the coldest air advection occurs over the Barents Sea. It is interesting to note that in
307   winter the criteria (7) is almost identical to simply $I_{cao} > 0$. The latter serves as a measure of the dry hydrostatic
308   stability of the layer between the ocean surface and the 700 hPa surface. Thus, positive values of I_{cao} indicate
309   conditions favorable for the mixed-layer development to the heights over 700 hPa. During strong background
310   advection mixed-layer can reach such heights only at a significant distance from the ice edge (Chechin and Lüpkes,
311   2017).
312
313   **3. Results**
314   **3.1 Wave climate and storm activity**
315   First, we consider the main features of wave conditions and wave climate in the Barents Sea, which directly
316   affect the processes of heat exchange in the ocean-atmosphere system. In Figure 3 4 the average significant wave
317   heights for the entire simulation period from 1979 to 2017 is shown. The highest average wave heights are found in
318   the western part of the sea. Here we can expect the greatest influence of sea waves on heat fluxes. In the north, due to
319   the presence of ice, the average wave heights do not exceed 1 m.
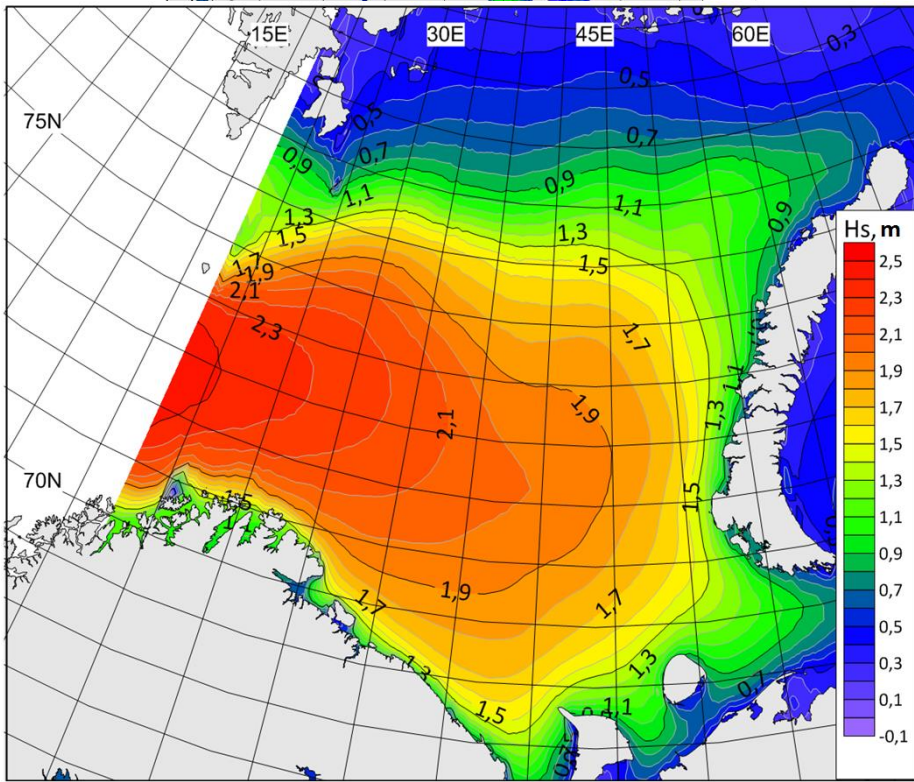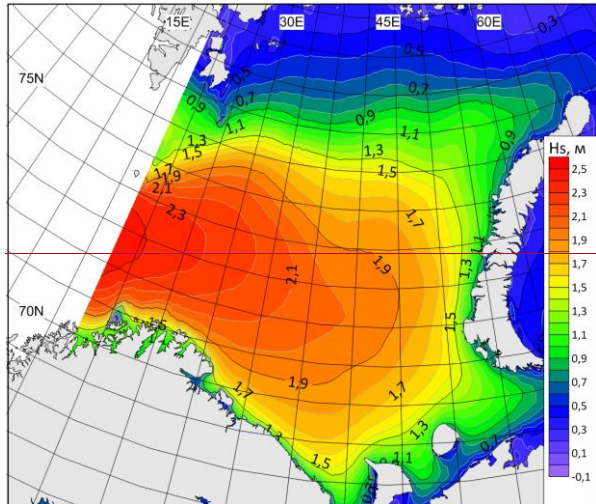
Figure 34. Long-term average significant wave height in the Barents Sea based on the WWIII simulation results for the all period 1979-2017.

325   Also, an equally important parameter is the wavelength, which is used in the parametrizations O2 and D3. In

326   Figure 4 5 the mean long-term spectral peak wavelength is shown. The wavelengths 80-100 m are observed in the

327   central and western parts of the Barents Sea. The results on the average wave height and wavelength in general are

328   consistent with similar works by other authors (Semedo et al., 2011; Stopa et al., 2016). Estimates of storm activity

329   based on such long-term analysis are relatively rare and their detailed analysis would require their detailed analysis is

330   necessary an additional research.

331
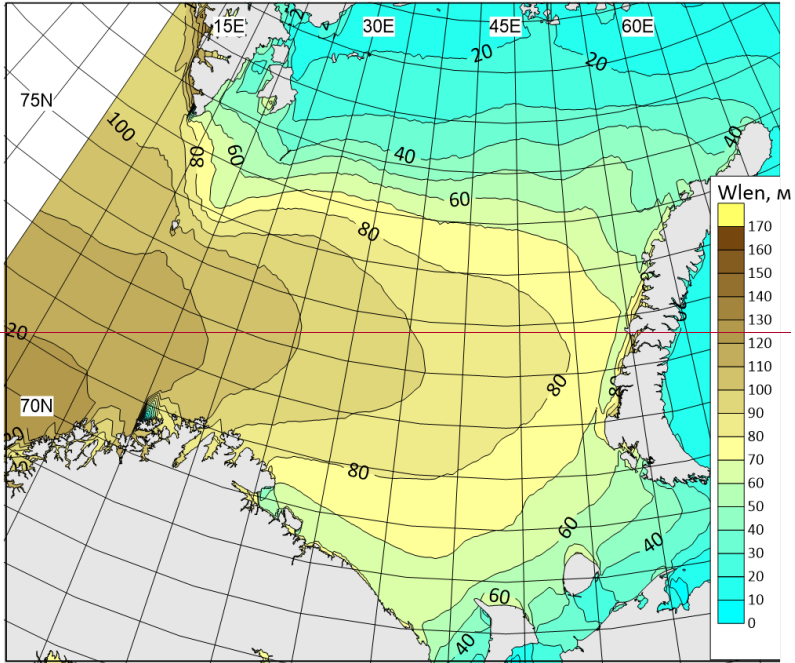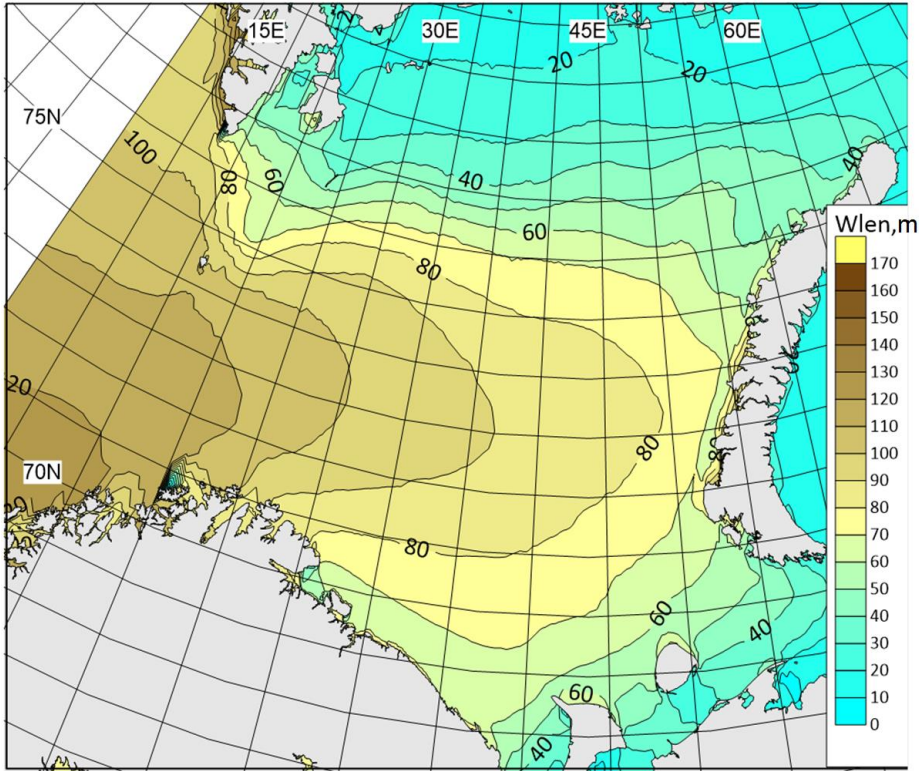
Figure 45. Long-term average long-term spectral peak wavelength in the Barents Sea based on the WWIII simulation results for the all period 1979-2017.

The Barents Sea is characterized by a high frequency of storm wave events, which provide a long swell in the extinction stage (i.e., "old seas") and limit the applicability of the Charnock formula. As shown in (Myslenkov et al., 2018), the number of storms per year in the Barents Sea can differ significantly. Figure 5 6 shows the number of storms calculated according to the wave model results with wave heights of more than 5 m and more than 7 m (identified as described in the Section 2.1). During the period from 1979 to 2017, several maxima of storm activity were observed, for example, in 1989-1991 and in 2011. Especially for these periods, the calculated heat fluxes are expected to be sensitive to the used of parameterizations of the roughness length (see Section 3.5).

343
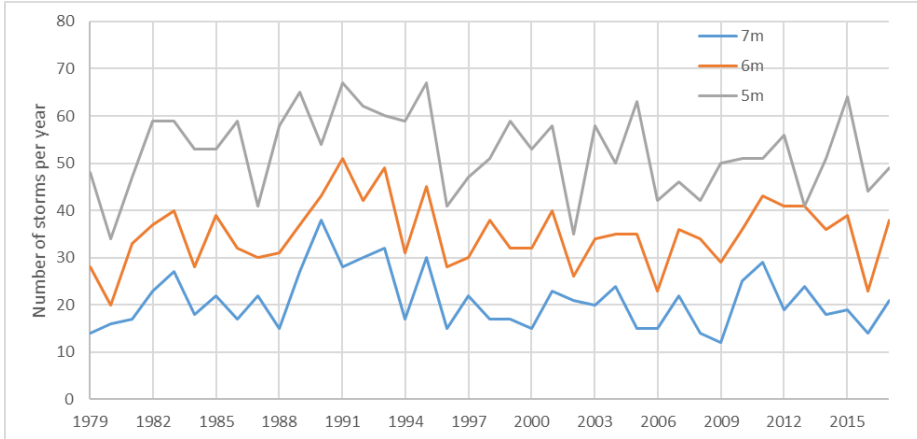
Figure 56. The number of storms with a significant wave height of more than 5, 6 and 7 m according to the WWIII simulation results for the period 1979-2017.

3.2 CAOs frequency of occurrence

Figure 6-7 shows the timeseries of the number of days with extreme CAOs selected using criteria formula (7) for each cold period (November-April) of 1979-2018. On average, CAOs are observed in 16.4 % days. However, the interannual variability of the frequency of occurrence of CAOs is large. Namely, the interannual standard deviation of the number of CAO days amounts to 12 days. Thereby, the number of CAO days per cold season varies from 6 in 2011-2012 to 56 in 1980-1981.

353
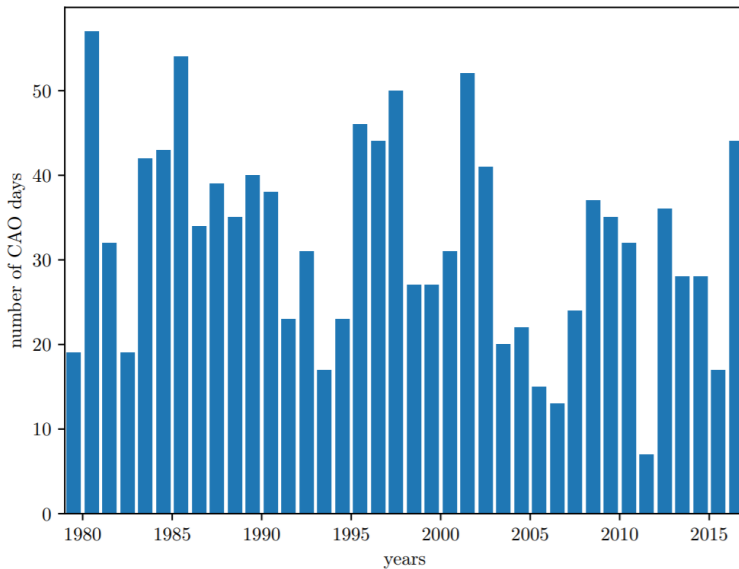
Figure 67. The number of days with CAOs over the Barents Sea selected using criteria formula (7) for each cold season in 1979-2018.

356

357   The frequency of occurrence of CAOs over the Barents Sea is governed by the variability of the largescale
358 patterns of atmospheric circulation. To the largest extent, the frequency of CAOs is correlated with the so-called
359 «Barents Oscillation» (Skeie et al., 2000; Wu et al. 2006; Kolstad et al., 2009). The latter is the mode of variability of
360 the sea-level pressure field represented by a dipole with high pressure over Greenland and Iceland and low pressure
361 over the northern part of the European part of Russia. Such pressure field promotes intense cold-air advection over the
362 Barents Sea from the north. Moreover, there is a negative correlation between the North Atlantic Oscillation index and
363 CAOs frequency of occurrence (Kolstad et al., 2009). Such a correlation is particularly strong for easterly CAOs,
364 which is obviously associated with the reduced strength of the westerlies.

365   A slight negative trend of the CAO days is seen in Figure 7. To a large extent, it can be explained by an
366 increase of the mean CAO index values over the Barents Sea. Such an increase can be associated either with a higher
367 air temperature over the Arctic in winter, i.e. CAOs become less severe, or with a decrease of the frequency of
368 synoptic patterns favorable for CAOs (Papritz and Grams, 2018). A negative trend of the CAO index values over the
369 Barents and Kara seas was also obtained by Narizhnaya et al. (2020) based on the ERA Interim data for the 1979-
370 2018 period. They found an increase of the number of weak and moderate CAOs and a decrease of the number of
371 strong CAOs.
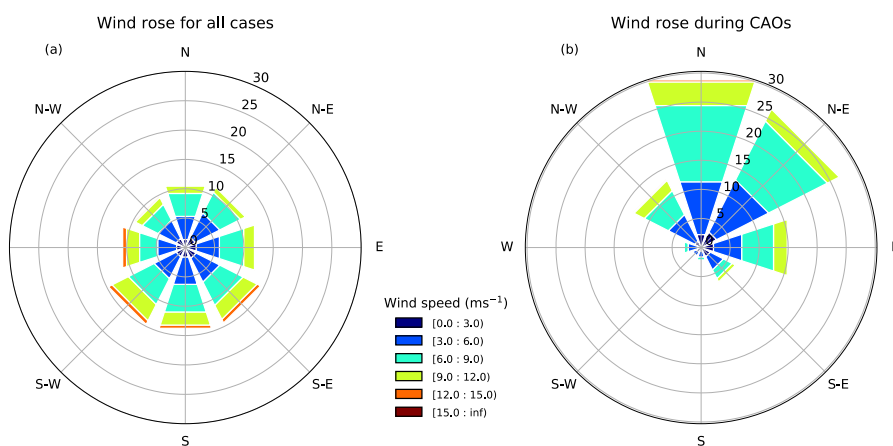
372
373
374   Figure 78. Frequency of occurrence of daily 10 m wind speed and direction, averaged over the ice-free part
375 of the Barents Sea for the period November-April 1979-2018 for all cases (a) and cold-air outbreaks (b).
376

377   The frequency of CAOs with easterly wind over the Barents Sea is significant and amounts represent up to
378 16% of all CAOs (Figure 7b8b). During CAOs, the highest frequency of occurrence have northerly (30%) and north-
379 easterly (27%) winds. The wind rose in CAOs differs from the wind rose in all cases during the cold season (Figure
380 7a8a). In particular, the prevailing wind direction over the Barents sea in winter is from the south. Moreover, the
381 winds having southerly and westerly components are the strongest.

382   The CAOs role in the heat exchange between the Barents Sea and the atmosphere is demonstrated by Figure
383 89. The latter shows the turbulent fluxes of sensible and latent heat, H and LE, respectively, the net longwave
384 radiative flux LW_{net}, and the total heat flux $F_{total} = H + LE + LW_{net}$ averaged over the November-April period over
385 the ice-free part of the Barents Sea as functions of the number of CAO days during the same period. Clearly, there is a

386 strong dependency of the Barents Sea on the number of CAO days. The highest correlation coefficients are obtained

387 for LW_{net}, F_{total} and H amount to 0.86, 0.85 and 0.84, respectively. A smaller correlation coefficient of 0.78 is

388 obtained for LE. Also, the coefficients of linear regression shown in Figure 8 9 demonstrate that F_{total} has the

389 strongest dependency on the number of CAO days. From all terms of the surface heat balance, the sensible heat flux H

390 is most sensitive to the number of CAO days. All the three considered components of the surface heat balance (H, LE

391 and LW_{net}) manifest heat loss from the sea surface to the atmosphere and are of comparable magnitude of about 70

392 Wm^{-2} on average.
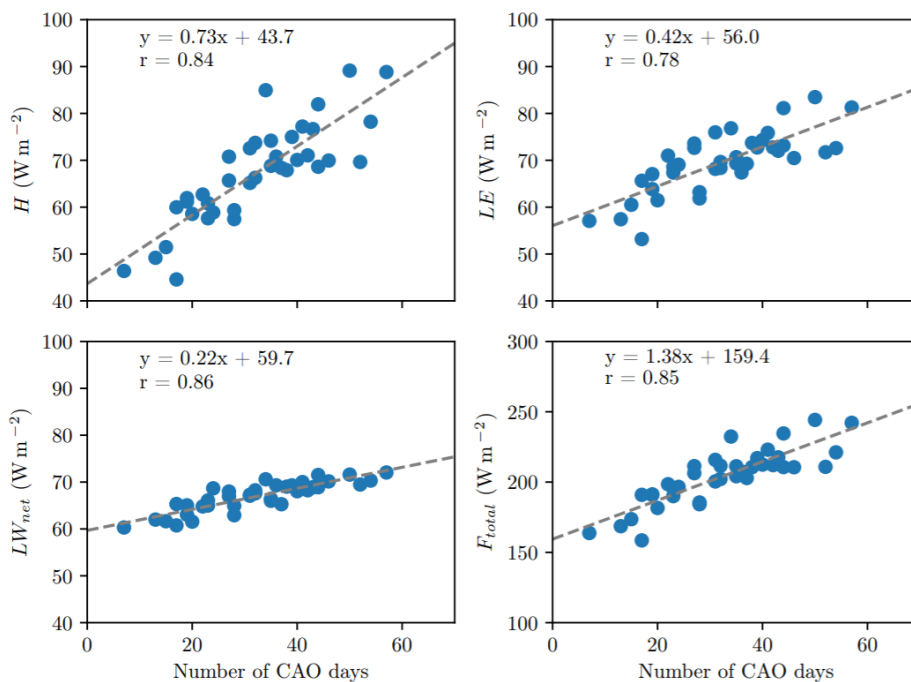
393

394 Figure 8 9. Turbulent fluxes of sensible and latent heat, H и LE respectively, net longwave radiative flux

395 LW_{net} and the total heat flux $F_{total} = H + LE + LW_{net}$ averaged over the cold season (November-April) and over the

396 ice-free part of the Barents Sea as function of number of CAO days during the same period for 1979-2018. Dashed

397 line shows the linear regression line, whose equation is given at each plot, as well as the correlation coefficient r.

398

399 We stress that the values of fluxes shown in Figure 8 9 are averaged over the ice-free part of the Barents Sea.

400 It is important to keep in mind that there is a large interannual variability of the area of sea ice cover in the Barents

401 Sea. This is another important factor, along with the number of CAO days, influencing the heat loss.

402 One might also expect that the ice edge retreat further north leads to a larger fetch over which the cold air

403 mass is advected. This would result in a higher air temperature over the Barents Sea which can locally decrease the

404 surface heat flux (Pope et al., 2020). However, this would lead to an increase of the total heat loss at the surface of the

405 Barents Sea which is proportional to the open water area. Since the sensible heat flux maximum during CAOs is

406 located near the ice edge, the maximal heat loss location would also shift further north. This might have implications

407 for the so-called "atlantification" in the northeastern part of the Barents Sea (e.g., Barton et al., 2018).

408

3.3 Verification of the COARE algorithm by the ship observations

Figure 19 0 shows the comparison of sensible and latent heat fluxes from shipborne observations and calculated using different roughness parameterizations, namely Charnock, 1955 (C55), Taylor and Yelland, 2001 (T1), Oost et al., 2002 (O2) and Drennan et al., 2003 (D3). Left side of FigureFig. 109 presents calculations made on the basis of reanalysis, interpolated to cruise track, while right side of the figure presents calculations from shipborne observations of meteorological parameters and radiative fluxes (available only in 2013-2015).

415

416
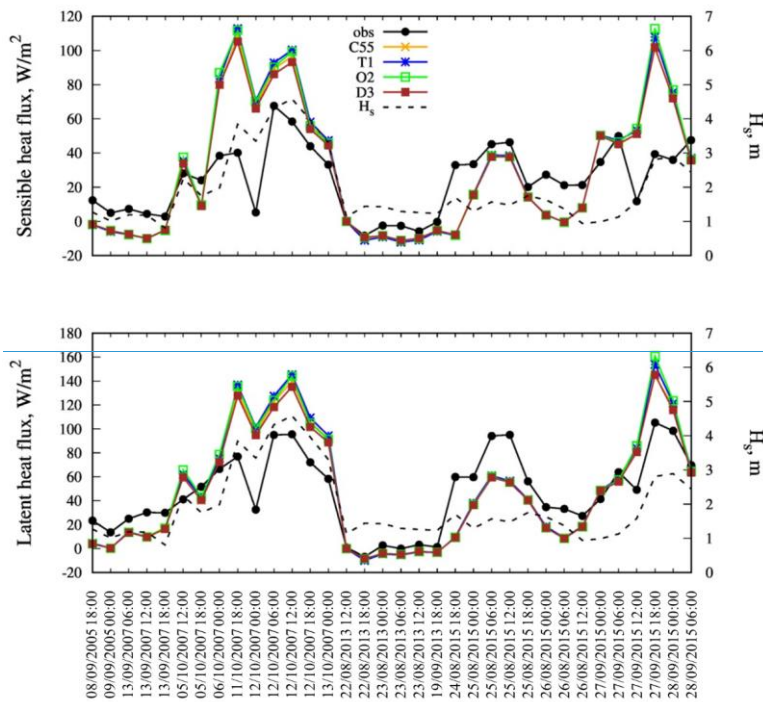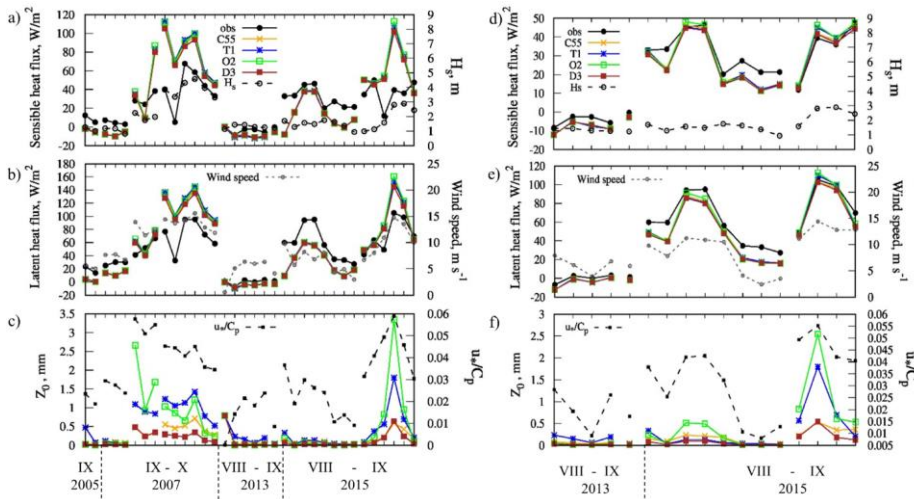
417 Figure 10~~9~~. Sensible (~~top~~a, d) and latent (~~bottom~~b, e) heat fluxes and roughness length (c, f) according to
418 NABOS observations (black solid line) and calculated using various roughness parameterizations (color solid lines).
419 Calculations are made on the basis of reanalysis (a-c) and observational data (d-f) (where observations of wind speed,
420 temperature and radiative fluxes are available). Also significant wave height H_s from WWIII simulations (a-d), wind
421 speed from reanalysis (b) and observations (e) and inverse wave age u_*/c_p (c, f) are shown. ~~The dashed line shows~~
422 ~~the significant wave height H_s according to WWIII simulations.~~

423

424 ~~Heat fluxes calculated with different roughness parameterizations are almost identical (Figure 9); an average~~
425 ~~difference between them is 1 W m⁻².~~ The correlation coefficient between the observed and the calculated fluxes from
426 reanalysis data ~~fluxes~~ (Figure ~~9~~10 a,b) is 0.7 for the sensible heat flux and 0.8 for the latent heat flux. However, the
427 mean absolute error (MAE) is rather large - about 20 W m^{-2}. The error magnitude increases with the increase of the
428 heat flux magnitude. The error may be connected both with the COARE algorithm itself and with the input data (i.e.,
429 related to the quality of meteorological parameters in the reanalysis). For example, a strong overestimation of heat
430 fluxes on October 11–12, 2007 is associated with the overestimation of wind speed (by 6–8 m s^{-1}) compared to
431 observations.

432 In order to estimate the accuracy of the COARE algorithm itself and to exclude the reanalysis error, we
433 additionally performed calculations on the basis of shipborne meteorological observations (Figure ~~9~~10d-f). In these
434 calculations we set precipitation intensity at zero and boundary layer height at 600 m, since these parameters were not
435 observed. The correlation coefficient between the observed and the calculated fluxes from observational data is 0.98-
436 0.99; MAE is reduced to ~ 4 W m^{-2} for sensible heat flux and to ~ 8 W m^{-2} for latent heat flux. ~~we excluded from the~~
437 ~~analysis those samples for which the reanalysis errors were large, namely, when the wind speed error exceeded 4 m s⁻¹~~
438 ~~and/or the SST and air temperature error exceeded 1.5 °C and/or the error in specific humidity exceeded 0.7 · 10⁻³ kg~~
439 ~~kg⁻¹. For such a sample, MAE decreased by half, to 10 W m⁻². For those periods when the error of wind speed,~~
440 ~~temperature, and specific humidity was the smallest, an error in the resulting heat fluxes also becomes small and~~
441 ~~amounts to about 5 W m⁻², which is most likely associated with the inaccuracy of the COARE algorithm. However,~~
442 ~~t~~This error is within the accuracy of the eddy-covariance method. The accuracy of this method in the case of ship

443 measurements can be significantly reduced due to the influence of air flow distortion by the ship. Therefore, we can
444 conclude that the calculated fluxes are in good agreement with the observations. ~~It should be noted that the error~~
445 ~~between the observed and calculated fluxes for all parameterizations exceeds the difference between calculated fluxes~~
446 ~~using different parameterizations.~~

447 Heat fluxes calculated with different roughness parameterizations are almost identical (Figure ~~9~~10); an
448 average difference between them is 1 W m^{-2}. This difference is maximal in October 2007 and September 2015 (up to
449 11% of the heat fluxes magnitudes~~values~~) when inverse wave age (Figure ~~9~~10c,f) is greater than 0.05, which is a
450 threshold for the young sea. Calculated roughness length (Figure ~~9~~10c,f) differs by up to 7 times for those cases.
451 However, most cases are characterised by developed sea situation ($u_*/c_p < 0.05$), when all parametrizations should
452 behave well (Drennan et al. 2005). And this must be the reason for small differences in roughness length and heat
453 fluxes. The small difference between parametrizations makes it impossible to unambiguously define the
454 parametrization that fits observations better.

456 **3.4 Long-term mean turbulent heat fluxes**

457 Here we consider the mean long-term values of heat fluxes calculated from the CFSR reanalysis data using
458 COARE algorithm and various roughness parameterizations. The mean long-term (~~for the period~~ 1979-2017) sensible
459 and latent heat flux obtained in the experiment C55 and the differences ~~in the~~ between ~~different~~ experiments shown on
460 Figure ~~10~~11, ~~11~~12. The main conclusion of these results is the presence of positive difference for T1 and O2
461 experiments and negative for D3. The long-term values of difference are~~is~~ small: 1-2 W m^{-2} for T1 and 0.5-1 W m^{-2}
462 for O2.
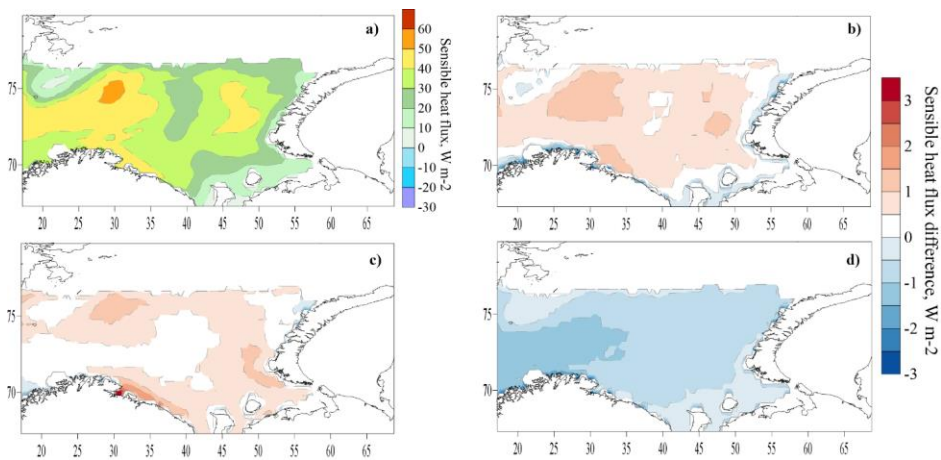
464 Figure ~~10~~11. Mean sensible heat flux in the experiment C55 (a,) and the difference in the sensible heat fluxes
465 between experiments T1 - C55 (b), O2 - C55 (c) and D3 - C55 (d). All grid nodes where sea ice was in more than half
466 of the cases are filtered.
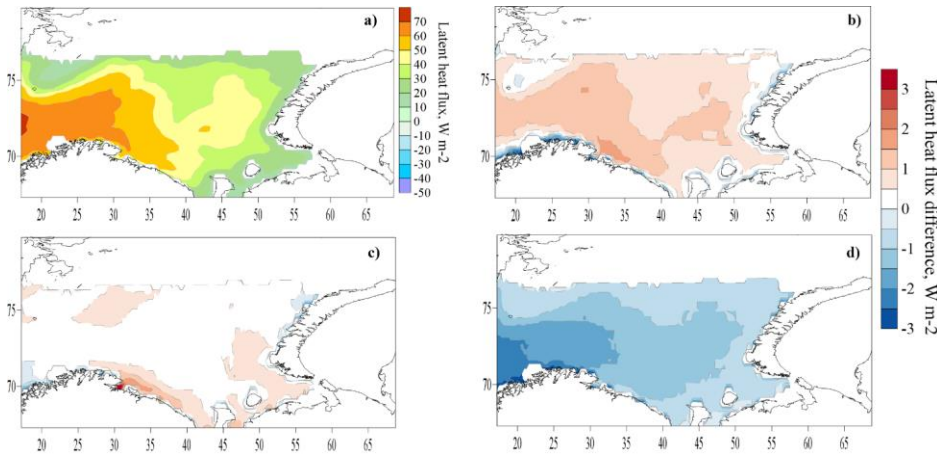
467

468   Figure ~~11~~12. Mean latent heat flux in the experiment C55 (a,) and the difference in the latent heat fluxes

469 between experiments T1 - C55 (b), O2 - C55 (c) and D3 - C55 (d). All grid nodes where sea ice was in more than half

470 of the cases are filtered.

471

472   Tables 1, 2 show the average statistics: the difference in heat fluxes with and without explicit accounting for

473 sea waves parameters. Over the entire Barents Sea, the full range of differences in the fluxes are small, within -3 ÷ ~ 2

474 W m^{-2}, which is only 1-3% of the mean absolute value. The greatest mean difference for sensible heat flux observed

475 for T1 and for latent heat flux for O2 parametrization.

476   The flux difference can exceed 30-50 W m^{-2} (in 0.1% of cases or 99.9 percentile) and in some extreme cases

477 reach 100-250 W m^{-2}. The highest maxima of the flux difference are obtained for the experiment O2.

478

479 **Table 1**

480   Statistical characteristics of the difference in the sensible heat flux calculated with and without explicit

481 accounting for sea waves parameters: mean difference, relative mean (ratio of the mean difference to the mean value

482 of the flux), mean absolute difference, 95 and 99.9 percentile and the maximum difference for the Barents Sea

	Mean difference (W m^{-2})	Relative mean difference (%)	Mean absolute difference (W m^{-2})	95 percentile (W m^{-2})	99.9 percentile (W m^{-2})
T1 - C55	0.5	1.4	1.7	7.3	40
O2 - C55	0.6	2.1	1.6	6.7	56
D3 - C55	-0.7	-2.3	1.1	3.7	35

483

484 **Table 2**

485   Statistical characteristics of the difference in the latent heat flux calculated with and without explicit

486 accounting for sea waves: mean, relative mean (ratio of the mean difference to the mean value of the flux), mean

487 absolute difference, 95 and 99.9 percentile and the maximum difference for the Barents Sea

	Mean difference (W m⁻²)	Relative mean difference (%)	Mean absolute difference (W m⁻²)	95 percentile (W m⁻²)	99.9 percentile (W m⁻²)
T1 - C55	0.7	1.6	1.8	6.7	41
O2 - C55	0.6	1	1.7	6.4	50
D3 - C55	-1.1	-2.8	1.3	3.7	38

The greatest differences between the experiments are found in those areas where the highest values of the heat fluxes are observed. This can be explained by the power-law dependence of the roughness length on the friction velocity / wave height. Moreover, in the O2 parameterization, the proportionality coefficient is larger (a2 = 4.5) than in the D3 parameterization (a3 = 3.4), which is reflected in the flux differences.

A more detailed spatial analysis of 99.9 percentile of sensible heat flux difference shown on Figure 1213. The extreme values of the flux difference taking O2-C55 difference as an example showed that some of the extrema are associated with coastal areas, mainly off the western coast of Novaya Zemlya during bora. Other extremes were associated with deep cyclones in different parts of the sea, with different distances from the coast. Some extremes are associated with storm waves or are observed immediately after storms, during cold-air outbreaks in the rear of cyclones. Therefore, the characteristics of heat fluxes during storm waves and cold-air outbreaks will be considered separately in the following sections.
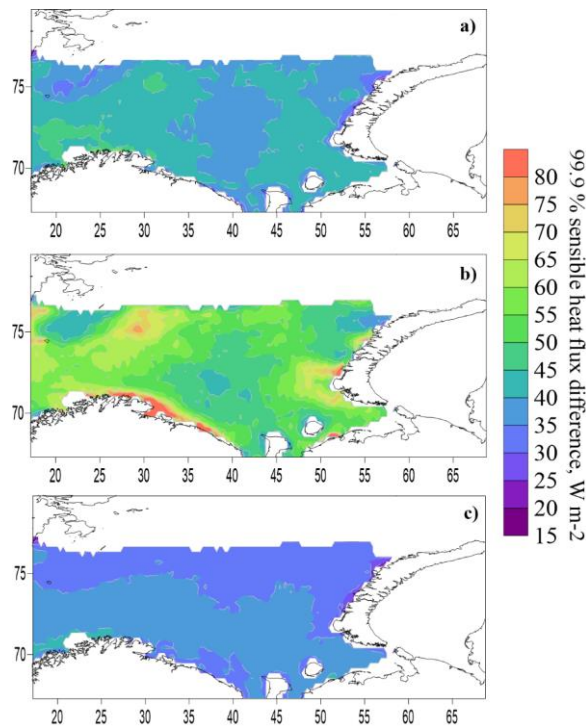
Figure 1213. 99.9 percentile of sensible heat flux difference between experiments T1 - C55 (a), O2 - C55 (b)

502   and D3 - C55 (c)

503

3.5 Turbulent heat fluxes during storm wave events

505   Here we consider turbulent heat fluxes during the storms identified in Section 3.1 (a total of 1964 days with

506   storms for the period 1979-2017). The spatial distribution of heat fluxes during storms (Figure 1314, 1415) resembles

507   the average distribution (Figure 1011, 1112), but the absolute values increase by almost a factor of 2. The average

508   sensible heat flux has several maxima - in the northwest of the sea, near the coast of the Kola Peninsula and a less

509   pronounced local maximum off the southern island of Novaya Zemlya. The flux difference between the experiments

510   is also distributed the same as on average and increases in absolute value (except for experiment D3). The average

511   flux difference between experiments reaches 4-5 W m^{-2} for T1-C55, 8 W m^{-2} for O2-C55 and 3-4 W m^{-2} for D3-C55.

512   On average, the relative difference in heat fluxes is 3% for T1-C55 and 3-5% for O2-C55. The correlation coefficient

513   between the magnitude of the flux and the magnitude of the flux difference is 0.9. For the D3 experiment, the flux

514   difference gradually increases from east to west, and some special structure associated precisely with storms does not

515   appear. The detected maxima of flux difference in the western part of Sea generally correspond to the maxima of the

516   average wave height (Figure 34).

517   It can be concluded that the mean pattern of heat fluxes in the Barents Sea is largely contributed by storms.
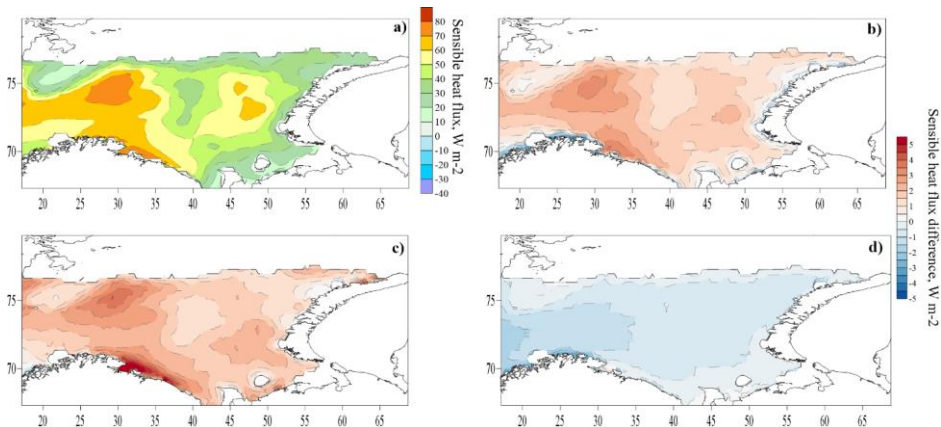
519   Figure 1314. Mean sensible heat flux in experiment C55 (a) and the flux difference in experiments T1 - C55

520   (b), O2 - C55 (c) and D3 - C55 (d) during storms.

521
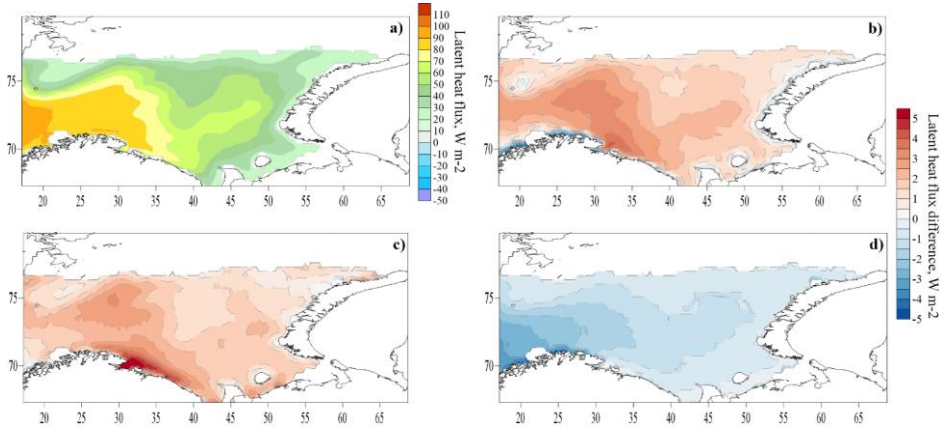
522
523   Figure ~~14~~15. Mean latent heat flux in experiment C55 (a) and the flux difference in experiments T1 - C55
524   (b), O2 - C55 (c) and D3 - C55 (d) during storms.
525

3.6 Turbulent heat fluxes during the cold-air outbreaks

527   Here we consider turbulent heat fluxes during cold-air outbreaks identified in Section 3.2 (2326 days with
528   cold-air outbreaks for the period 1979-2017). The average values of the sensible heat flux increase, especially in the
529   northwestern part (2 times compared with the average), during cold-air outbreaks (Figure ~~15a~~16a). The spatial
530   distribution of the latent heat flux is almost the same with the average one, but the flux magnitude increases by 1.5
531   times (~~Figure16a~~Figure17a).
532   Experiments T1 and O2 increase everywhere ~~provide to increase~~ the magnitude~~s~~ of the sensible and latent
533   heat fluxes compared to C55 during cold-air outbreaks (Figure ~~15~~16, ~~16~~17). Explicit accounting for the storm wave
534   events leads to an increase in heat fluxes mainly in the northwest of the sea and near the ice edge. But the differences
535   between the experiments are still small - on average less than 4 W m^{-2} for the sensible heat flux and less than 2.5 W
536   m^{-2} for the latent heat flux, i.e. less than 3-4% of flux magnitudes (Figure ~~15~~16, ~~16~~17). At the same time, the extreme
537   values of the flux difference during cold-air outbreaks, as for storm waves, are several times smaller than when
538   considering long-term means.
539   The average values of the flux difference during cold-air outbreaks are smaller than during storms, but the
540   extreme values during cold-air outbreaks and during storms are close.
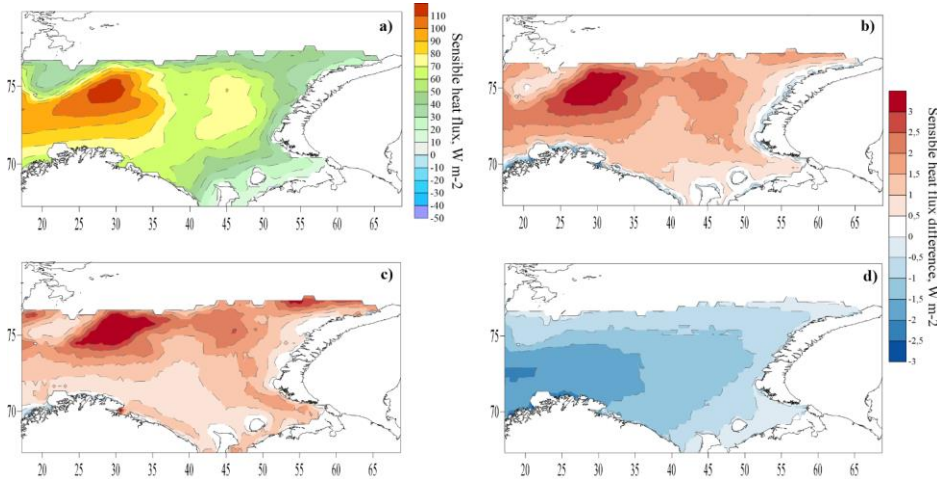
Figure 1516. Mean sensible heat flux in experiment C55 (a) and the flux difference in experiments T1 - C55 (b), O2 - C55 (c) and D3 - C55 (d) during cold-air outbreaks.
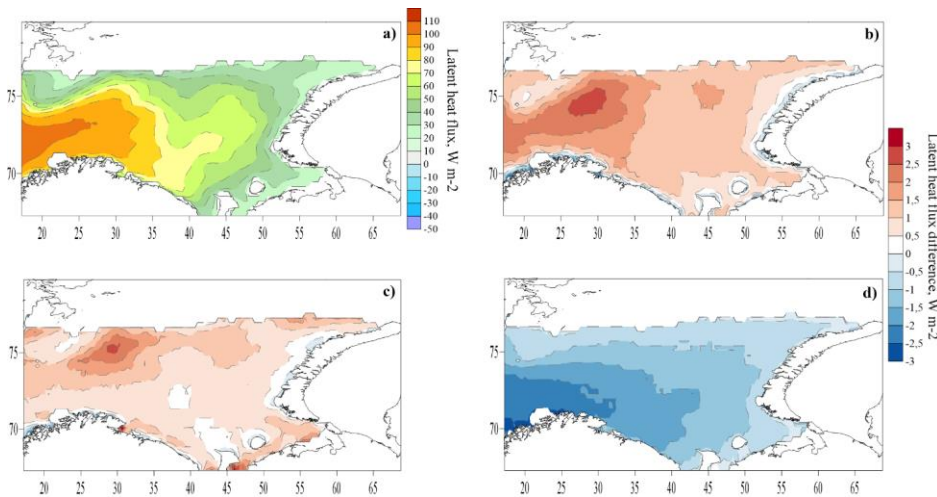
Figure 1617. Mean latent heat flux in experiment C55 (a) and the flux difference in experiments T1 - C55 (b), O2 - C55 (c) and D3 - C55 (d) during cold-air outbreaks.

3.7 Turbulent heat fluxes during the simultaneously observed storm waves and cold-air outbreaks

Finally, we consider cases when cold-air outbreaks and storm wave events were simultaneously observed (a total of 292 days for the period 1979-2017) (Figure 1718, 1918). The magnitude of the heat fluxes and the difference between the experiments in these cases are the largest in comparison with other situations. The sensible heat flux in experiment C55 reaches 170 W m^{-2} (in the north-west of the sea), the latent heat flux is 140 W m^{-2} (in the west). The average difference T1-C55 reaches 6 W m^{-2} for sensible heat flux and 4.5 W m^{-2} for latent heat flux. The average difference O2-C55 reaches 10 W m^{-2} for sensible heat flux and 7 W m^{-2} for latent heat flux. The average difference

556 D3-C55 reaches 3 W m^{-2} in the west of the sea.

557   The extreme values of the difference, which can reach 700 W m^{-2}, are also greatest in the case of
558 simultaneously observed storms and cold-air outbreaks. Figure ~~19~~ 20 shows case when the difference in sensible heat
559 fluxes exceeded 100 W m^{-2} between C55 and T1 parametrizations and 400 W m^{-2} between C55 and O2
560 parametrizations. The greatest difference is noted for the eastern local maximum of the heat flux. There, the wind was
561 blowing from the south-east (on the front side of the cyclone) and reached 15-20 m/s; however, wave height and
562 especially wave length were rather low due to short fetch. The storm cyclone was moving very fast over the Barents
563 Sea, which resulted in fast changes of wind direction and velocity in the eastern side of the sea. Thus, it was a very
564 young sea state that resulted in such a difference between parametrizations. ~~associated with the cold-air outbreak~~
565 ~~during the north-eastern wind.~~ An analysis of other cases, in which extreme values of the flux difference were
566 observed, also showed the presence of two local maxima (western and eastern) of heat fluxes. The same maxima also
567 appear in the long-term mean pattern of heat fluxes (Figure ~~15~~16, ~~16~~17) and are associated with the cyclone structure
568 and sea ice edge configuration: strong south-easterly winds in front of the cyclone and northerly winds in the rear both
569 produce young waves on short fetches, that contribute much to augmented roughness and heat fluxes.
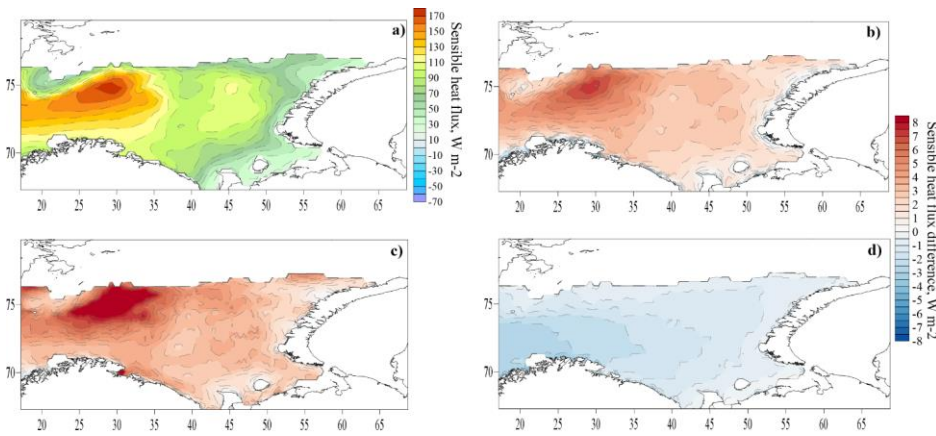
571   Figure ~~17~~18. Mean sensible heat flux in experiment C55 (a) and the flux difference in experiments T1 - C55
572 (b), O2 - C55 (c) and D3 - C55 (d) during storms and cold-air outbreaks.
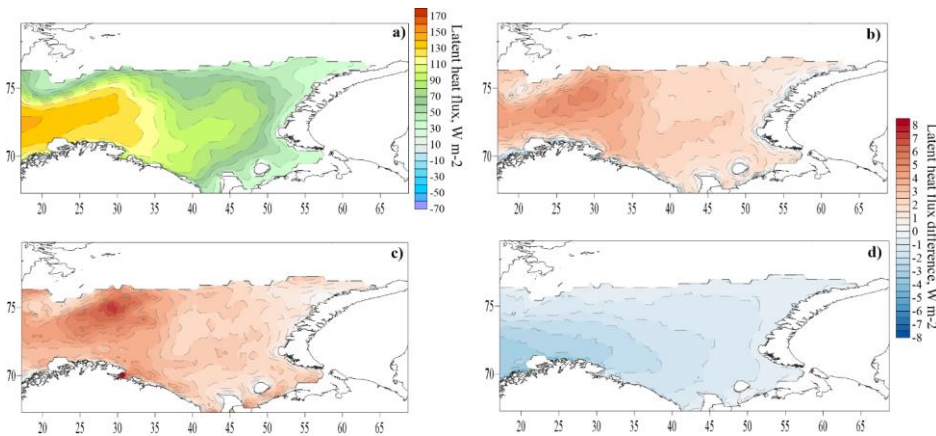
574   Figure ~~18~~19. Mean latent heat flux in experiment C55 (a) and the flux difference in experiments T1 - C55
575   (b), O2 - C55 (c) and D3 - C55 (d) during storm waves and cold-air outbreaks.

576
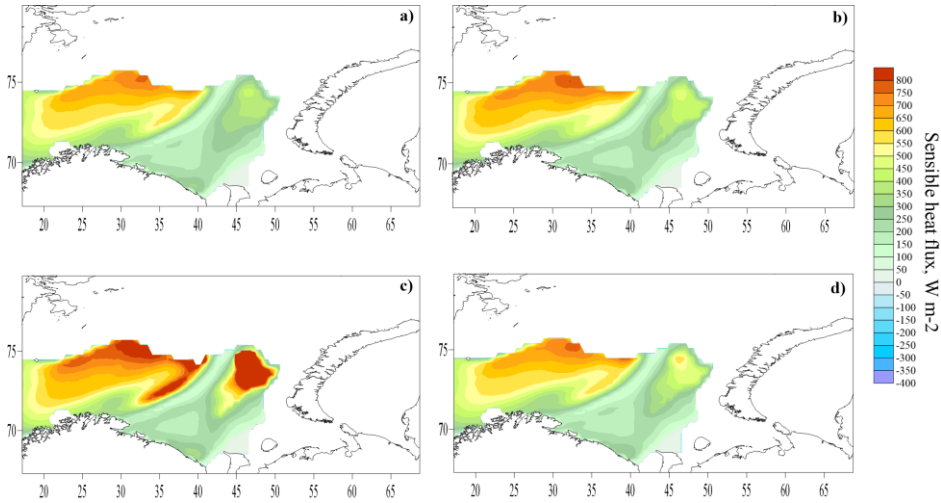
577   Figure ~~19~~20. Sensible heat fluxes at 00 UTC January 13, 2003 calculated with C55 (a), T1(b), O2(c) and
578   D3(d) parametrizations.

579

580   **4. Discussion and conclusions**

581   This paper presents the results of turbulent heat flux calculations in the Barents Sea using the COARE
582   algorithm, meteorological data from reanalysis and sea-wave data from retrospective simulations with the ~~WW3~~
583   WWIII wave model. The calculations were performed for several options: using the modified Charnock
584   parameterization of roughness length (C55) and using the explicit accounting for the sea waves parameters in the
585   roughness parametrizations T1 (Taylor and Yelland), O2 (Oost et al.) and D3 (Drennan et al.). Particular attention was
586   paid to the episodes with extremely intense energy exchange between the atmosphere and the ocean: storms and cold-
587   air outbreaks (CAOs).

588   We obtained the mean annual distribution of the height and wavelength in the Barents Sea from wave
589   modelling results. Estimates of the storm activity from 1979 to 2017 were also obtained, confirming its high
590   interannual variability. Based on the data of wave modeling, a catalog of storm waves with the wave height exceeding
591   5 m was created. This catalog was used to calculate heat fluxes during storms.

592   The catalog of extreme CAOs over the Barents Sea was also obtained. It is shown that the extreme CAOs are
593   observed in 16.4% of days of a cold season (November-April). However, the number of CAO days varies from 6 in
594   2011-2012 to 56 in 1981-1982 manifesting large interannual variability. The important role of CAOs in the energy
595   exchange of the Barents Sea and the atmosphere is demonstrated. A high correlation was found between the number
596   of CAO days and turbulent fluxes of sensible and latent heat, as well as with the net flux of long-wave radiation
597   averaged over the ice-free surface of the Barents Sea during a cold season. Thus, the significant interannual variability
598   of the frequency of occurrence of CAOs largely determines the interannual variability of heat loss from the ice-free
599   surface of the Barents Sea.

600   Comparison of the calculated heat fluxes with ship observations during the NABOS expeditions was carried
601   out. Significant part of the errors in determining the heat fluxes is associated not with the used COARE algorithm, but

with discrepancies in meteorological parameters reproduced by the CFSR reanalysis and locally observed on the ship. ~~Excluding samples with big errors in meteorological parameters, we~~We ~~obtain~~ estimated the algorithm error ~~of about~~as ~~5~~104 W m^{-2} for sensible heat flux and 8 W m^{-2} for latent heat flux, which is within the accuracy of the eddy-covariance method during ship measurements.

The differences between the experiments (long-term calculations for the period 1979-2017) with different parameterizations of the roughness length are small and are on average 1-3% of the flux magnitude. In some cases, differences can reach 100-200 W m^{-2}. Parameterizations of Taylor and Yelland (2001) and Oost et al. (2002), which represent the dependence of the roughness length on wave steepness and wave length, respectively, on average overestimate the magnitude of the fluxes, and the parameterization of Drennan et al. (2003) (the dependence of the roughness length on wave height and wave age) steadily underestimates the magnitude of the fluxes over the entire sea compared to the Charnock parameterization. Thus, the effect of explicit accounting for wave parameters is~~, on average,~~ small when time averaging is performed and multidirectional, depending on the used parameterization. The modified Charnock formula quite successfully describes the real behavior of the surface roughness even without explicitly taking into account the waves parameters. This can be explained, firstly, by the Charnock parameter dependence on various ranges of wind speed obtained from empirical data, and secondly, by the high correlation between wave parameters and wind speed usually observed. Therefore, in climate studies operating with large time-scales and spatially and temporally averaged values~~In the climatic aspect~~, it can be argued that explicit accounting for sea waves in the calculations of heat fluxes can be neglected.

However, in some situations, the choice of a particular roughness parameterization may be important. During storms and cold-air outbreaks, differences between parameterizations increases along with the turbulent heat transfer increase. In some extreme cases, during storms and cold-air outbreaks, the difference T1-C55 reaches 100 W m^{-2}, the difference O2-C55 exceeded~~reaches~~ 700 W m^{-2}. O2 parametrization gives the highest values of heat fluxes and roughness length among other parametrizations, and in some cases (in cases of very young sea) calculated values do not correspond to reality. For instance, sensible heat flux reached 1300 W m^{-2} and roughness length reached 7 m in the case, shown on Figure ~~19~~20. For the same case, roughness length reached only 2 mm in C55 calculations, 1 cm in T1 calculations and 5 cm in D3 calculations. Though D3 parametrization depends on the wave age as well as O2 parametrization, the degree of dependence in the former is lower than in the latter.

The difference between the experiments with parameterization D3 and C55 is almost the same in all cases and always decreases (modulo) from west to east of the sea, actually resembling the mean distribution of wave height. Experiments with parameterizations T1 and O2 deviate most strongly from the Charnok parametrization in those areas and at those times when the absolute values of the fluxes are large. The greatest absolute difference between the fluxes is obtained for the simultaneous action of storms and cold-air outbreaks in the northwest and northeast of the sea, i.e. when the values of the fluxes are the greatest and sea state is young. The relative flux difference (the difference normalized to the value of the flux) over the entire sea is greatest during storms (in some areas more than 5%) (Figure ~~20~~21), but in some areas (in the north, near the ice edge), the relative difference is higher at the simultaneous action of cold-air outbreaks and storms. In all situations, the relative difference is large in the region of the Pechora Sea due to the low absolute values of the fluxes. An area of low absolute and relative values of the flux difference is located to the north-east from Bear Island.
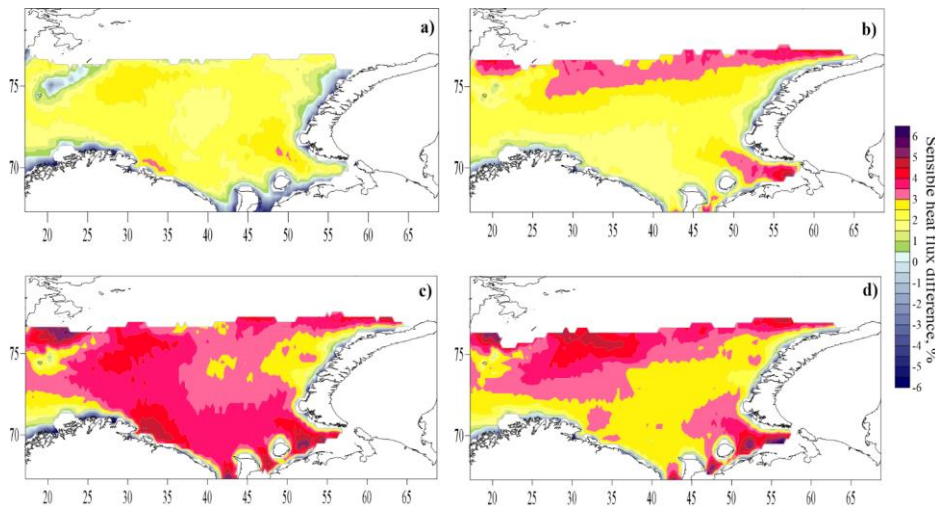
Figure 2021. Mean relative difference in sensible heat flux (%) in the experiments T1 - C55 for all cases (a), during cold-air outbreaks (b), during storms (c) and during simultaneously observed storm waves and cold-air outbreaks (d).

Finally, based on the results of our study we can recommend the use of the parametrizations that take into account the wave parameters explicitly on small time scales, for example, in weather prediction, in the Barents Sea region. This is especially true in the case of storms, cold-air outbreaks, and especially in the case of simultaneous action of storms and cold-air outbreaks, in case of relatively short fetches and young sea state especially in the northern half of the sea, near the ice edge, in the Pechora Sea and near the coast of the Kola Peninsula (in case of storms). However, we cannot recommend any particular parametrization due to the lack of in-situ observations in those areas and those times, where heat flux differences in parametrizations are big. Our results highlighted the fact that one should be cautious when using Oost et al. (2002) parametrization in young sea state conditions.

All the conclusions made are valid when turbulent heat fluxes are under consideration. Obviously, differences in the roughness length between calculations with different parametrizations have a more explicit and strong effect on the momentum flux. Although the latter was not the object of this study, nevertheless, its values were estimated as well, and mean relative differences in momentum flux between parametrizations reached 100% of the momentum flux valuemagnitude. Thus, the choice of the parametrization is a key factor in the momentum air-sea exchange applications.

Data availability

Data and results in this article resulting from numerical simulations are available upon request from the corresponding author.

Author contributions

The concept of the study was jointly developed by SM. SM did the numerical simulations, analysis, visualization and manuscript writing. ASh did the Coare simulations and its visualization. DCh did the calculations of cold-air outbreaks repeatability.

Competing interests.

The authors declare that they have no conflict of interest.

669   **Acknowledgments.**

670   Data analysis funded by the RFBR (project 18-05-60083 Shestakova A.A. and Chechin D.G.). The wave

671   modeling was done with the financial support of the RFBR (project 20-35-70039 Myslenkov S.A.). Authors gratefully

672   thank I.A. Repina for the provided shipborne observations collected during NABOS expeditions.

673

674   **References**

675   Andreas, E. L.: Thermal and size evolution of sea spray droplets (No. CRREL-89-11). Cold Regions
676   Research and Engineering Lab Hanover NH, 1989.
677   Arthun, M., Schrum, C.: Ocean surface heat flux variability in the Barents Sea. Journal of Marine Systems,
678   83(1-2), 88-98, https://doi.org/10.1016/j.jmarsys.2010.07.003, 2010.
679   Barton, B. I., Lenn, Y., & Lique, C.: Observed Atlantification of the Barents Sea Causes the Polar Front to
680   Limit the Expansion of Winter Sea Ice, Journal of Physical Oceanography, 48(8), 1849-1866, 2018.
681   Beljaars, A. C. M., & Holtslag, A. A. M.: Flux parameterization over land surfaces for atmospheric models.
682   Journal of Applied Meteorology, 30(3), 327-341, https://doi.org/10.1175/1520-
683   0450(1991)030%3C0327:FPOLSF%3E2.0.CO;2, 1991.
684   Brodeau, L., Barnier, B., Gulev, S. K., & Woods, C.: Climatologically significant effects of some
685   approximations in the bulk parameterizations of turbulent air–sea fluxes. Journal of Physical Oceanography, 47(1), 5-
686   28, https://doi.org/10.1175/JPO-D-16-0169.1, 2017.
687   Brümmer, B.: Boundary-layer modification in wintertime cold-air outbreaks from the Arctic sea ice. Bound.-
688   Layer Meteor. 80, 109–125, 1996.
689   Brunke, M. A., Wang, Z., Zeng, X., Bosilovich, M., & Shie, C. L.: An assessment of the uncertainties in
690   ocean surface turbulent fluxes in 11 reanalysis, satellite-derived, and combined global datasets. Journal of Climate,
691   24(21), 5469-5493, https://doi.org/10.1175/2011JCLI4223.1, 2011.
692   Brutsaert, W.: Evaporation into the Atmosphere—Theory, History, and Applications. D. Reidel, 299 pp, 1982.
693   Chechin D.G, Lüpkes C., Repina I.A., Gryanik V.M.: Idealized dry quasi-2D mesoscale simulations of cold-
694   air outbreaks over the marginal sea-ice zone with fine and coarse resolution. J. Geophys. Res., 118, pp. 8787-8813,
695   doi: 10.1002/jgrd.50679, 2013.
696   Chechin D.G., Zabolotskikh E.V., Repina I.A., Shapron B.: Influence of baroclinicity in the atmospheric
697   boundary layer and Ekman friction on the surface wind speed during cold-air outbreaks in the Arctic, Izv. Atmos.
698   Ocean. Phys., Vol. 51 No. 2, pp. 127–137, doi: 10.1134/S0001433815020048, 2015.
699   Chechin D.G, Lüpkes C.: Boundary-layer development and low-level baroclinicity during high-latitude cold-
700   air outbreaks: a simple model. Boundary-Layer Meteorol 162: 91. https://doi.org/10.1007/s10546-016-0193-2, 2017.
701   Chechin, D. G. and Lüpkes, C.: Baroclinic low-level jets in Arctic marine cold-air outbreaks. IOP Conference
702   Series: Earth and Environmental Science, IOP Publishing, 231, 012011, 2019.
703   Charles, E., Hemer, M.: Parameterization of a wave-dependent surface roughness: A step towards a fully
704   coupled atmosphere-ocean-sea ice-wave system. In 13th International Workshop on Wave Hindcasting and
705   Forecasting and 4th Coastal Hazard Symposium, 2013.
706   Charnock, H.: Wind stress on a water surface. Quarterly Journal of the Royal Meteorological Society,
707   81(350), 639-640, 1955.
708   Drennan, W. M., Graber, H. C., Hauser, D. and Quentin, C.: On the wave age dependence of wind stress over
709   pure wind seas. Journal of Geophysical Research, 108(C3), 8062, 2003.
710   Drennan, W. M., Taylor, P. K., and Yelland, M. J.: Parameterizing the sea surface roughness. Journal of
711   physical oceanography, 35(5), 835-848, 2005.
712   ECMWF: Part VII: ECMWF wave model. IFS Documentation Cy31r1, 56 pp. [Available online at
713   http://www.ecmwf.int/research/ifsdocs/CY31r1/WAVES/IFSPart7.pdf.], 2007.
714   Fairall, C. W., Bradley, E. F., Hare, J. E., Grachev, A. A., & Edson, J. B.: Bulk parameterization of air–sea
715   fluxes: Updates and verification for the COARE algorithm. Journal of climate, 16(4), 571-591,
716   https://doi.org/10.1175/1520-0442(2003)016%3C0571:BPOASF%3E2.0.CO;2, 2003.
717   Fairall, C. W., Bradley, E. F., Rogers, D. P., Edson, J. B., & Young, G. S.: Bulk parameterization of air-sea
718   fluxes for tropical ocean-global atmosphere coupled-ocean atmosphere response experiment. Journal of Geophysical
719   Research: Oceans, 101(C2), 3747-3764, https://doi.org/10.1029/95JC03205, 1996.
720   Fletcher, J., S. Mason, and C. Jakob: The Climatology, Meteorology, and Boundary Layer Structure of
721   Marine Cold Air Outbreaks in Both Hemispheres. J. Climate, **29**, 1999–2014, https://doi.org/10.1175/JCLI-D-15-
722   0268.1, https://doi.org/10.1175/JCLI-D-15-0268.1, 2016.
723   Grachev, A.A., Fairall, C.W. & Bradley, E.F.: Convective Profile Constants Revisited. Boundary-Layer
724   Meteorology 94(3): 495-515, 2000.
725   Grønas A., Skeie P.: A case study of strong winds at an Arctic front. Tellus 51:865–879,
726   https://doi.org/10.3402/tellusa.v51i5.14498, 1999.
727   Häkkinen, S., Cavaleri, D. J.: A study of oceanic surface heat fluxes in the Greenland, Norwegian, and
728   Barents Seas. Journal of Geophysical Research: Oceans, 94(C5), 6145-6157,

729 https://doi.org/10.1029/JC094iC05p06145, 1989.

730 Hasselmann, S., and K. Hasselmann: Computations and parameterizations of the nonlinear energy transfer in
731 a gravity-wave spectrum, Part I: A new method for efficient computations of the exact nonlinear transfer integral. J.
732 Phys. Oceanogr. 15, 1,369–1,377, 2018.

733 Ivanov, V., Varentsov, M., Matveeva, T., Repina, I., Artamonov, A., & Khavina, E.: Arctic Sea Ice Decline in
734 the 2010s: The Increasing Role of the Ocean—Air Heat Exchange in the Late Summer. Atmosphere, 10(4), 184, 2019.

735 Ivanov V. V., Timokhov L.A.: Atlantic water in the arctic circulation transpolar system. Russian Meteorology
736 and Hydrology. Vol. 44, no. 4. 238–249, https://doi.org/10.3103/S1068373919040034, 2019.

737 Janssen, P. A.: Quasi-linear theory of wind-wave generation applied to wave forecasting. Journal of physical
738 oceanography, 21(11), pp. 1631-1642, https://doi.org/10.1175/1520-
739 0485(1991)021%3C1631:QLTOWW%3E2.0.CO;2, 1991.

740 Jones, I. S., Toba, Y. (Eds.).:Wind stress over the ocean. Cambridge University Press, 2001.

741 Kaimal, J. C., Wyngaard, J. C., Izumi, Y., and Cote 0. R.: Spectral Characteristics of Surface-Layer
742 Turbulence. Quart. J. Roy. Meteorol. Soc. 98, 563-589, 1972.

743 Kim, T., Moon, J. H., Kang, K.: Uncertainty and sensitivity of wave-induced sea surface roughness
744 parameterisations for a coupled numerical weather prediction model. Tellus A: Dynamic Meteorology and
745 Oceanography, 70(1), 1-18, https://doi.org/10.1080/16000870.2018.1521242, 2018.

746 Kolstad E. W., Bracegirdle T.J.: Marine cold-air outbreaks in the future: an assessment of IPCC AR4 model
747 results for the Northern Hemisphere. Clim. Dyn. 30:871–885. doi:10.1007/s00382-007-0331-0,
748 https://doi.org/10.1007/s00382-007-0331-0, 2008.

749 Kolstad, E.W., Bracegirdle, T.J. and Seierstad, I.A.: Marine cold-air outbreaks in the North Atlantic: temporal
750 distribution and associations with large-scale atmospheric circulation. Clim Dyn 33, 187–197, doi:10.1007/s00382-
751 008-0431-5, 2009.

752 Kolstad E.W.: Extreme small-scale wind episodes over the Barents Sea: When, where and why? Clim Dyn,
753 45, 2137-2150, doi:10.1007/s00382-014-2462-4, 2015.

754

755 Large W. G. and S. G. Yeager: The global climatology of an interannually varying air-sea flux data
756 set. Climate Dynamics, 33, 341-364 (DOI: 10.1007/s00382-008-0441-3), 2009.

757 Li Jingkai, Ma Y, Liu Q, Zhang W and Guan C: Growth of wave height with retreating ice cover in the
758 Arctic. Cold Regions Science and Technology, 164, 102790. doi: 10.1016/j.coldregions.2019.102790, 2019.

759 Liu, W. T., Katsaros, K. B., & Businger, J. A.: Bulk parameterization of air-sea exchanges of heat and water
760 vapor including the molecular constraints at the interface. Journal of the Atmospheric Sciences, 36(9), 1722-1735,
761 1979.

762 Liu Q., Babanin A., Zieger S., Young I., Guan C.: Wind and wave climate in the Arctic Ocean as observed by
763 altimeters. J. Climate. 2016. V. 29(22). P. 7957–7975, https://doi.org/10.1175/JCLI-D-16-0219.1, 2016.

764 Mahrt, L., Vickers, D., Frederickson, P., Davidson, K., & Smedman, A. S.: Sea-surface aerodynamic
765 roughness. Journal of Geophysical Research: Oceans, 108(C6), https://doi.org/10.1029/2002JC001383, 2003.

766 Moore G.W.K.: The Novaya Zemlya Bora and its impact on Barents Sea air-sea interaction, Geophys. Res.
767 Lett., 40, 3462 — 3467, doi:10.1002/grl.50641, 2013.

768 Myslenkov S., Medvedeva A., Arkhipkin V., Markina M., Surkova G., Krylov A., Dobrolyubov S.,
769 Zilitinkevich S., Koltermann P.: Long-term statistics of storms in the Baltic, Barents and White Seas and their future
770 climate projections. Geography, Environment, Sustainability.V. 11. № 1. P. 93–112, https://doi.org/10.24057/2071-
771 9388-2018-11-1-93-112, 2018.

772 Myslenkov S.A., Arkhipkin V.S., Koltermann K.P.: Evaluation of swell height in the Barents and White
773 Seas, Moscow University Bulletin, Series 5. Geography. №5, pp.59-66, 2015.

774 Myslenkov, S.A., Markina, M.Yu., Arkhipkin, V.S., Tilinina, N.D.: Frequency of storms in the Barents sea
775 under modern climate conditions. Vestnik Moskovskogo Universiteta, Seriya 5: Geografiya. Volume, Issue 2, 2019,
776 Pages 45-54, 2019.

777 Myslenkov S.A., Markina M. Yu., Kiseleva S.V. et al.: Estimation of Available Wave Energy in the Barents
778 Sea. Thermal Engineering. 65, 7, 411–419, https://doi.org/10.1134/S0040601518070054, 2018.

779 Narizhnaya A.I., Chernokulsky A.V., Akperov M.G., Chechin D.G., Esau I., Timazhev A.V.: Marine cold air
780 outbreaks in the Russian Arctic: climatology, interannual variability, dependence on sea-ice concentration. IOP Conf.
781 Ser.: Earth Environ. Sci. 606 012039, https://doi.org/10.1088/1755-1315/606/1/012039, 2020.

782 Oost, W. A., Komen, G. J., Jacobs, C. M. J., & Van Oort, C.: New evidence for a relation between wind
783 stress and wave age from measurements during ASGAMAGE. Boundary-Layer Meteorology, 103(3), 409-438, 2002.

784 Pan, Y., Sha, W., Zhu, S., Ge, S.: A new parameterization scheme for sea surface aerodynamic roughness.
785 Progress in Natural Science, 18(11), 1365-1373, https://doi.org/10.1023/A:1014913624535, 2008.

786 Papritz, L. and T. Spengler: A Lagrangian Climatology of Wintertime Cold Air Outbreaks in the Irminger
787 and Nordic Seas and Their Role in Shaping Air–Sea Heat Fluxes. J. Climate, 30, 2717–2737,
788 https://doi.org/10.1175/JCLI-D-16-0605.1, 2017.

789 Papritz, L. and Grams, C. M.: Linking low-frequency large-scale circulation patterns to cold air outbreak
790 formation in the north- eastern North Atlantic. Geophysical Research Letters, 45, 2542–2553.
791 https://doi.org/10.1002/2017GL076921, 2018.

Pithan, F. , Svensson, G. , Caballero, R. , Chechin, D. , Cronin, T. W. , Ekman, A. M. L. , Neggers, R. , Shupe, M. D. , Solomon, A. , Tjernström, M. and Wendisch, M.: Role of air-mass transformations in exchange between the Arctic and mid-latitudes , Nature Geoscience, 11 (11), pp. 805-812, https://doi.org/10.1038/s41561-018-0234-1, 2018.

Pope, J.O., Bracegirdle, T.J., Renfrew, I.A. et al.: The impact of wintertime sea-ice anomalies on high surface heat flux events in the Iceland and Greenland Seas. Clim Dyn 54, 1937–1952. https://doi.org/10.1007/s00382-019-05095-3, 2020.

Prakash, K. R., Pant, V., Nigam, T.: Effects of the Sea Surface Roughness and Sea Spray-Induced Flux Parameterization on the Simulations of a Tropical Cyclone. Journal of Geophysical Research: Atmospheres, 124(24), https://doi.org/10.1029/2018JD029760, 2019.

Rahmstorf, S., Ganopolski, A.: Long-Term Global Warming Scenarios Computed with an Efficient Coupled Climate Model. Climatic Change 43, 353–367. https://doi.org/10.1023/A:1005474526406, 1999.

Renfrew, I. A., Moore, G. K., Guest, P. S., & Bumke, K.: A comparison of surface layer and surface turbulent flux observations over the Labrador Sea with ECMWF analyses and NCEP reanalyses. Journal of Physical Oceanography, 32(2), 383-400, https://doi.org/10.1175/1520-0485(2002)032%3C0383:ACOSLA%3E2.0.CO;2, 2002.

Ribal, A., Young, I.R.: 33 years of globally calibrated wave height and wind speed data based on altimeter observations. Sci Data 6, 77. https://doi.org/10.1038/s41597-019-0083-9, 2019.

Saha S. et al.: The NCEP climate forecast system reanalysis. Bul. of the American Meteorological Society. V. 91. № 8. P. 1015–1057, https://doi.org/10.1175/2010BAMS3001.1, 2010.

Saha S. et al.: The NCEP Climate Forecast System Version 2. J. Climate. 27, 2185—2208, https://doi.org/10.1175/JCLI-D-12-00823.1, 2014.

Savijärvi H. I.: Cold air outbreaks over high-latitude sea gulfs, Tellus A: Dynamic Meteorology and Oceanography, 64:1, DOI: 10.3402/tellusa.v64i0.12244, 2012.

Semedo A, Sušelj K, Rutgersson A, Sterl A.: A global view on the wind sea and swell climate and variability from ERA-40. J Clim 24(5):1461–1479, https://doi.org/10.1175/2010JCLI3718.1, 2011.

Shimura, T., Mori, N., Takemi, T., Mizuta, R.: Long-term impacts of ocean wave-dependent roughness on global climate systems. Journal of Geophysical Research: Oceans, 122(3), 1995-2011, https://doi.org/10.1002/2016JC012621, 2017.

Simonsen, K., Haugan, P. M.: Heat budgets of the Arctic Mediterranean and sea surface heat flux parameterizations for the Nordic Seas. Journal of Geophysical Research: Oceans, 101(C3), 6553-6576, https://doi.org/10.1029/95JC03305, 1996.

Skeie P.: Meridional flow variability over the Nordic Seas in the Arctic Oscillation framework. Geophys. Res. Lett. 27:2569-2572. https://doi.org/10.1029/2000GL011529, 2000.

Smedsrud, L. H., et al.: The role of the Barents Sea in the Arctic climate system, Rev. Geophys., 51, 415–449, doi:10.1002/rog.20017, 2013.

Smith, S. D.: Coefficients for sea surface wind stress, heat flux, and wind profiles as a function of wind speed and temperature. Journal of Geophysical Research: Oceans, 93(C12), 15467-15472, 1988.

Stopa J., Ardhuin F.,Girard-Ardhuin F.: Wave climate in the Arctic 1992-2014: seasonality and trends. Cryosphere, 10(4), pp.1605-1629, https://doi.org/10.5194/tc-10-1605-2016, 2016.

Taylor, P. K., & Yelland, M. J.: The dependence of sea surface roughness on the height and steepness of the waves. Journal of physical oceanography, 31(2), 572-590, https://doi.org/10.1175/1520-0485(2001)031%3C0572:TDOSSR%3E2.0.CO;2, 2001.

Tolman, H.: The WAVEWATCH III Development Group User Manual and System Documentation of WAVEWATCH III version 4.18. Tech. Note 316, NOAA/NWS/NCEP/MMAB, 2014, available at: http://polar.ncep.noaa.gov/waves/wavewatch/ manual.v4.18.pdf (last access: 23 June 2018), 2014.

Varentsov, M.I., Repina, I.A., Artamonov, A. Yu., Khavina, E.M., & Matveeva, T.A.: Experimental studies of energy transfer and the dynamics of the atmospheric boundary layer in the Arctic in the summer. Proceedings of the Hydrometeorological Research Center of the Russian Federation, (361), 95-127, 2016.

Wheeler, D. D., Harvey, V. L., Atkinson, D. E., Collins, R. L., and Mills, M. J.: A climatology of cold air outbreaks over North America: WACCM and ERA-40 comparison and analysis, J. Geophys. Res., 116, D12107, doi:10.1029/2011JD015711, 2011.

Wind and Wave Climate Handbook. Barents, Okhotsk, and Caspian Seas: Ed. by L. I. Lopatukhin, et al. (Russian Maritime. Register Shipping., St. Petersburg, 2003), 2003.

Wu, B., J. Wang, and J.E. Walsh: Dipole Anomaly in the Winter Arctic Atmosphere and Its Association with Sea Ice Motion. J. Climate, 19, 210–225, https://doi.org/10.1175/JCLI3619.1, 2006.

Yu, L., & Jin, X.: Satellite-based global ocean vector wind analysis by the Objectively Analyzed Air-sea Fluxes (OAFlux) Project: Establishing consistent vector wind time series from July 1987 onward through synergizing microwave radiometers and scatterometers (Vol. 1). WHOI OAFlux Tech. Rep. WHOI-OA-2011, 2011.

Zilitinkevich S.S., Grachev A.A., Fairall C.W.: Scaling reasoning and field data on the sea surface roughness lengths for scalars. J. Atmos. Sci. V. 58. P. 320–325, 2001.

Код поля изменен